remote sensing

MDPI

Article

Improvement and Validation of GOCI-II Surface Reflectance and Downstream Land Products

Sun-Hwa Kim *, Inkwon Baek, Daeho Seong, Jihyun Choi and Jeong Eun

PERPIXEL Inc., Incheon 21984, Republic of Korea; aaron77@perpixel.co.kr (I.B.); eoghs@perpixel.co.kr (D.S.); sally0@perpixel.co.kr (J.C.); eun2@perpixel.co.kr (J.E.)
* Correspondence: sunhk@perpixel.co.kr; Tel.: +82-32-811-7639

Highlights

What are the main findings?

- GOCI-II-specific 6SV atmospheric correction substantially reduced surface reflectance errors, particularly at shorter wavelengths, and the improvement persisted under common-pixel validation.
- Improved surface reflectance contributed to more accurate broadband albedo, NDVI, and EVI products across the GOCI-II land-processing chain.

What are the implications of the main findings?

- Sensor-specific post-launch refinement is important for ensuring the accuracy and consistency of geostationary land surface products.
- Reliable GOCI-II surface reflectance provides a stronger basis for high-frequency monitoring of terrestrial environments over East Asia.

Abstract

The Geostationary Ocean Color Imager-II (GOCI-II) provides high-frequency multispectral observations over East Asia, offering considerable potential for terrestrial monitoring. Surface reflectance (SR) is a fundamental land product that represents surface spectral properties after accounting for atmospheric effects and serves as a primary input to downstream products such as surface albedo and vegetation indices. Consequently, uncertainties in SR retrieval can propagate through the processing chain and affect the accuracy and consistency of these derived land products. However, the original GOCI-II land SR algorithm was developed before launch using GOCI proxy data and employed a temporal minimum-reflectance selection scheme, limiting its ability to fully account for the actual spectral, geometric, and atmospheric characteristics of GOCI-II observations. In this study, we developed and evaluated an improved GOCI-II-specific atmospheric correction framework based on a 6SV lookup table (LUT) constructed for all 12 reflective bands. The revised retrieval incorporates pixel-level observation geometry, aerosol optical depth, water vapor, ozone, and terrain elevation and produces observation-specific clear-sky SR without temporal minimum compositing. The original and improved land products were evaluated using all 12 Local Area slots throughout 2023. SR was validated against MODIS MCD19A1, broadband albedo against MODIS MCD43A3, and NDVI and EVI against MODIS MOD13Q1 and GK2A/AMI products. For SR, the largest improvements occurred at shorter wavelengths: RMSE decreased from 0.271 to 0.042 at 412 nm, from 0.196 to 0.032 at 443 nm, and from 0.134 to 0.036 at 490 nm. Improvements were also observed at longer wavelengths, and a common-pixel analysis confirmed that the reductions in bias and RMSE persisted when the original and improved products were evaluated using an identical set of valid pixels. The revised processing also improved the downstream land products. The RMSE of broadband

Check for updates

Academic Editor: Weizhen Hou

Received: 23 September 2026
Revised: 4 November 2026
Accepted: 4 November 2026
Published: 8 November 2026

Copyright: © 2026 by the authors. Licensee MDPI, Basel, Switzerland. This article is an open access article distributed under the terms and conditions of the Creative Commons Attribution (CC BY) license.

black-sky albedo decreased from 0.037 to 0.025, while that of white-sky albedo decreased from 0.039 to 0.035. For vegetation indices, NDVI RMSE decreased from 0.403 to 0.142 against MODIS MOD13Q1 and from 0.342 to 0.100 against GK2A/AMI, while EVI RMSE decreased from 0.274 to 0.111 and from 0.268 to 0.071, respectively. These results demonstrate that sensor-specific post-launch atmospheric correction substantially improves GOCI-II SR and that enhanced accuracy of this fundamental upstream product contributes to greater consistency and accuracy throughout the downstream GOCI-II land-product chain.

Keywords: GOCI-II; surface reflectance; atmospheric correction; 6SV; surface albedo; NDVI; EVI; geostationary satellite

1. Introduction

Satellite-based optical remote sensing provides spatially continuous observations of land surfaces and has become an essential source of information for monitoring vegetation, agriculture, land-cover change, and surface energy processes. Among satellite-derived land products, surface reflectance (SR) is a fundamental quantity representing the spectral characteristics of the land surface after atmospheric effects have been removed. Operational satellite missions such as MODIS and Landsat routinely provide atmospherically corrected SR products [1,2], which serve as the basis for higher-level products including surface albedo [3–5] and vegetation indices such as the normalized difference vegetation index (NDVI) and enhanced vegetation index (EVI) [6,7]. Similar land-product frameworks have also been established for other operational satellite missions [8]. Because these downstream products are derived directly or indirectly from atmospherically corrected reflectance, uncertainties in SR retrieval can propagate through the processing chain and affect the accuracy and consistency of subsequent land products. Previous research has also demonstrated that atmospheric correction methods can influence the comparability of NDVI derived from different satellite and unmanned aerial vehicle sensors, further emphasizing the importance of reliable SR retrieval for vegetation monitoring [9].

Accurate atmospheric correction is therefore a prerequisite for quantitative land remote sensing. The top-of-atmosphere (TOA) signal measured by a satellite sensor contains not only radiation reflected by the land surface but also contributions from molecular scattering, aerosol scattering and absorption, and gaseous absorption. Separating these atmospheric effects from the surface signal remains challenging because the retrieval is sensitive to aerosol properties, atmospheric composition, observation geometry, and surface anisotropy. Intercomparison efforts such as the Atmospheric Correction Inter-comparison eXercise (ACIX) have demonstrated that substantial differences can occur among atmospheric correction algorithms even when applied to the same satellite observations [10]. Physically based radiative-transfer models, particularly the Second Simulation of a Satellite Signal in the Solar Spectrum (6S) and its vector version (6SV), have therefore been widely used for satellite atmospheric correction [11,12]. Aerosol effects are particularly important in the visible wavelengths [13], and operational approaches commonly employ lookup tables (LUTs) or multi-angular retrieval strategies to efficiently account for varying atmospheric and geometric conditions [14,15]. Recent developments have further emphasized the importance of sensor-specific atmospheric correction strategies, accurate atmospheric parameter estimation, and comprehensive validation of surface reflectance products. The ACIX-II Land intercomparison evaluated 12 atmospheric correction processors for Landsat 8 and Sentinel-2, revealing differences in aerosol optical depth (AOD), water vapor, and SR retrieval performance among the processors [16]. An independent assessment of the MAJA atmospheric correction processor further demonstrated the importance of evaluating

aerosol estimation and accounting for the effects of adjacency and topographic corrections when assessing SR accuracy [17]. These studies indicate that the reliability of atmospheric correction depends not only on the radiative transfer model but also on the representation of atmospheric variability, sensor characteristics, and the procedures used to evaluate the resulting products.

Geostationary (GEO) satellites provide a distinctive opportunity for terrestrial remote sensing because they repeatedly observe the same region throughout the daytime, providing much denser temporal sampling than polar-orbiting satellites while maintaining an approximately fixed viewing geometry for a given ground location. These characteristics can increase the probability of obtaining cloud-free observations and provide additional temporal and angular information for separating atmospheric and surface signals [18–24]. For example, AERUS-GEO exploited multiple daily Meteosat/SEVIRI observations for aerosol and surface characterization [18], while land SR retrieval from Himawari-8 AHI demonstrated the potential of high-frequency GEO observations to provide substantially more daily valid observations than conventional polar-orbiting products [19]. More recently, GeoNEX-AC explicitly exploited the diurnal variability of GEO observations to retrieve atmospheric and surface properties [20]. Recent research using Himawari-8/9 AHI further demonstrated the feasibility of retrieving land SR through 6SV LUT-based atmospheric correction combined with ancillary atmospheric information and BRDF modeling, with evaluation against MODIS observations [21]. In addition, GEO–LEO intercomparison studies have highlighted the importance of accounting for observation geometry when evaluating geostationary SR, particularly at mid-latitudes [22]. High-frequency GEO observations have also demonstrated advantages for characterizing vegetation and land-surface seasonal dynamics [23]. Beyond SR retrieval, geostationary observations from GOES-R and Himawari have been used to derive land surface directional reflectance and albedo products, illustrating the broader potential of GEO measurements for monitoring surface radiative properties [24]. However, changing solar illumination during the day produces pronounced directional variations in land reflectance, requiring careful treatment of surface anisotropy and bidirectional reflectance distribution function (BRDF) effects [4,25,26]. Thus, GEO observations offer unique opportunities for high-frequency land monitoring but also impose sensor- and geometry-specific requirements on atmospheric correction and subsequent land-product retrieval. Recent research using the Geostationary Environmental Monitoring Spectrometer (GEMS) has demonstrated the utility of BRDF-based surface reflectance characterization for geostationary observations [27]. Furthermore, diurnal variations in solar illumination geometry have been shown to introduce directional effects into geostationary NDVI time series, potentially affecting vegetation phenology monitoring [28].

The Geostationary Ocean Color Imager (GOCI) demonstrated the potential of geostationary ocean-color sensors for terrestrial applications over East Asia. Although originally designed for ocean observations, its visible and near-infrared channels and high temporal sampling enabled monitoring of terrestrial reflectance and vegetation dynamics. GOCI-derived BRDF-adjusted NDVI captured crop seasonal development and provided additional cloud-free observations during the East Asian summer monsoon compared with MODIS [29]. High-frequency GOCI observations were also used to characterize surface BRDF and improve thin-cloud detection over land [30]. A subsequent study developed and evaluated a 6S-based atmospheric correction approach for GOCI land observations, demonstrating the feasibility of quantitative SR retrieval from geostationary ocean-color observations [31]. These studies established the potential of GOCI-type geostationary measurements for quantitative terrestrial applications while highlighting the importance of accurate surface characterization and atmospheric correction over East Asia, where aerosol effects can be substantial [31,32].

The Geostationary Ocean Color Imager-II (GOCI-II), onboard GEO-KOMPSAT-2B (GK2B), extends these capabilities with 12 reflective multispectral bands and a nominal spatial resolution of 250 m. However, the original GOCI-II land SR algorithm was developed before launch using GOCI observations as proxy data [31]. The original processing framework applied atmospheric correction followed by a temporal minimum-reflectance selection using observations from the current and preceding days. Although this strategy was designed to reduce residual atmospheric and cloud contamination, it does not fully exploit the actual post-launch spectral, radiometric, and observational characteristics of GOCI-II and may suppress genuine temporal changes in surface reflectance. While recent GEO studies have demonstrated the potential of sensor-specific atmospheric correction and observation-geometry-aware SR evaluation [21,22], the existing GOCI-II operational framework requires refinement to better represent the actual sensor characteristics and atmospheric conditions of individual observations. The availability of actual GOCI-II observations and corresponding atmospheric ancillary data after launch therefore provides an opportunity to refine the existing atmospheric correction framework and retrieve SR for individual observations without relying on temporal minimum-reflectance selection.

The importance of improving SR extends beyond the reflectance product itself because GOCI-II higher-level land products are generated sequentially from atmospherically corrected reflectance. According to the original GOCI-II BRDF/albedo/vegetation-index ATBD [33], SR is first used for BRDF modeling to generate fixed-viewing BRDF-adjusted reflectance (FVBAR). The resulting BRDF information is then used to derive narrowband and broadband surface albedo, while red, near-infrared, and blue FVBAR are used to calculate NDVI and EVI. Consequently, uncertainties introduced during atmospheric correction can propagate through the processing chain and affect multiple downstream land products. In the present study, the original BRDF modeling and vegetation-index formulations were retained, allowing changes in vegetation-index performance to be primarily associated with changes propagated from the upstream SR retrieval. For broadband albedo, however, the narrow-to-broadband conversion coefficients were additionally updated specifically for GOCI-II; therefore, changes in broadband albedo reflect the combined effects of improved SR and the revised conversion coefficients. Recent studies have further demonstrated the potential of high-frequency geostationary observations for retrieving vegetation structural parameters, including leaf area index and fractional vegetation cover, using radiative transfer modeling [34].

In this study, we improve and evaluate the existing atmospheric correction and SR retrieval framework for GOCI-II land observations. The principal modifications include (1) constructing a sensor-specific 6SV LUT for all 12 GOCI-II reflective bands using post-launch sensor characteristics; (2) extending the LUT interpolation procedure to five dimensions—solar zenith angle, viewing zenith angle, relative azimuth angle, AOD, and surface altitude—while incorporating pixel-level atmospheric information; and (3) replacing the original temporal minimum-reflectance selection with observation-specific clear-sky SR retrieval. These modifications are intended to improve the representation of atmospheric and geometric variability while preserving the temporal characteristics of individual GOCI-II observations.

The objectives of this study are therefore to (1) refine the existing GOCI-II atmospheric correction algorithm using post-launch sensor characteristics and pixel-level atmospheric information; (2) quantitatively evaluate the resulting SR against independent reference satellite products; and (3) assess how the improvement in SR is reflected in downstream BRDF-based albedo and vegetation-index products, while retaining the original BRDF and vegetation-index formulations and updating the narrow-to-broadband conversion coefficients for GOCI-II. By evaluating both the upstream SR and downstream products

within the same operational processing framework, this study examines how post-launch refinement of atmospheric correction can improve the accuracy and consistency of the GOCI-II terrestrial product chain.

2. Materials and Methods

2.1. Study Area and Datasets

2.1.1. GOCI-II Observations and Land Products

GOCI-II, onboard GEO-KOMPSAT-2B (GK2B), observes the East Asian region from geostationary orbit using 12 multispectral bands covering the visible to near-infrared wavelengths (380–865 nm), with a nominal spatial resolution of 250 m at nadir. The GOCI-II Local Area (LA) covers approximately 2500 × 2500 km and is divided into 12 observation slots (S000–S011), each consisting of 2780 × 2780 pixels (Table 1 and Figure 1). The 12 slots collectively cover East Asia, including the Korean Peninsula, Japan, eastern China, and adjacent regions (Figure 1).

Table 1. Characteristics of the GOCI-II sensor used in this study.

Category	Specification
Satellite	GEO-KOMPSAT-2B (GK2B)
Orbit	Geostationary (~36,000 km)
Payload	Geostationary Ocean Color Imager II (GOCI-II)
Spectral Bands	12 multispectral bands (VIS, NIR)
Band Center Wavelength Range	380–865 nm
Spatial Resolution (Nadir)	250 m
Swath	2500 km × 2500 km
Slot	12 slots (2780 × 2780 pixels per slot)
Temporal Resolution	1 h (10 observations/day, 23:15–08:15 UTC)
Radiometric Resolution	12 bits
Launch Date	19 Feb 2020

This study used GOCI-II observations acquired throughout 2023 over all 12 LA slots to evaluate the original and improved land products. The products evaluated include land surface reflectance (SRL), broadband and narrowband surface albedo (LSAB and LSAN), and vegetation indices (VI). SRL provides surface reflectance for the 12 GOCI-II spectral bands, LSAN provides band-specific black-sky and white-sky albedo, LSAB provides broadband black-sky and white-sky albedo, and the VI product contains NDVI and EVI. SRL is generated multiple times per day, whereas the albedo and VI products are generated once daily Table 3.

Both the original and improved GOCI-II products were included in the analysis to quantify the effects of the revised atmospheric correction on SR and its propagation to downstream land products. The BRDF modeling and vegetation-index formulations were retained from the original processing framework, whereas the narrow-to-broadband conversion coefficients used for broadband albedo retrieval were updated using GOCI-II-specific data. Accordingly, differences in the vegetation-index products primarily reflect changes propagated from the input surface reflectance, while differences in broadband albedo reflect the combined effects of improved surface reflectance and the updated narrow-to-broadband conversion. Because the validation datasets were derived from sensors with different spectral configurations, the spectral response functions (SRFs) of GOCI-II, MODIS, and GK2A/AMI were compared to identify spectrally corresponding bands and to account for inter-sensor spectral differences in subsequent analyses (Figure 2).

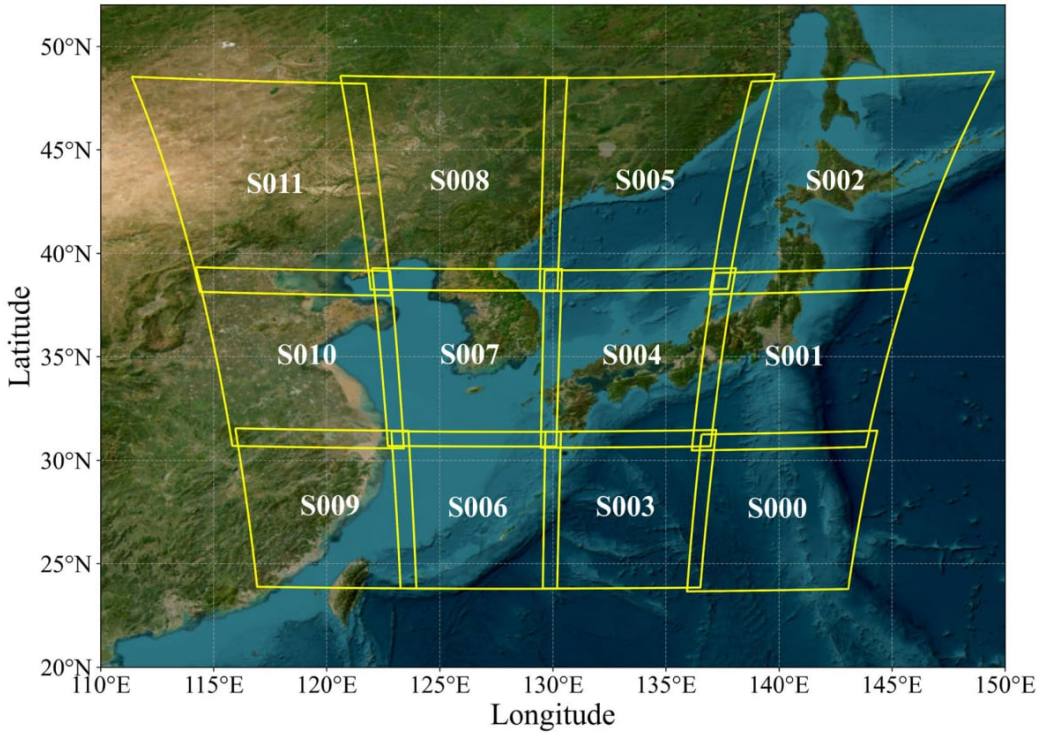


Figure 1. Spatial coverage of the GOCI-II Local Area and the configuration of its 12 observation slots (S000–S011) over East Asia. The background image is from Esri World Imagery.

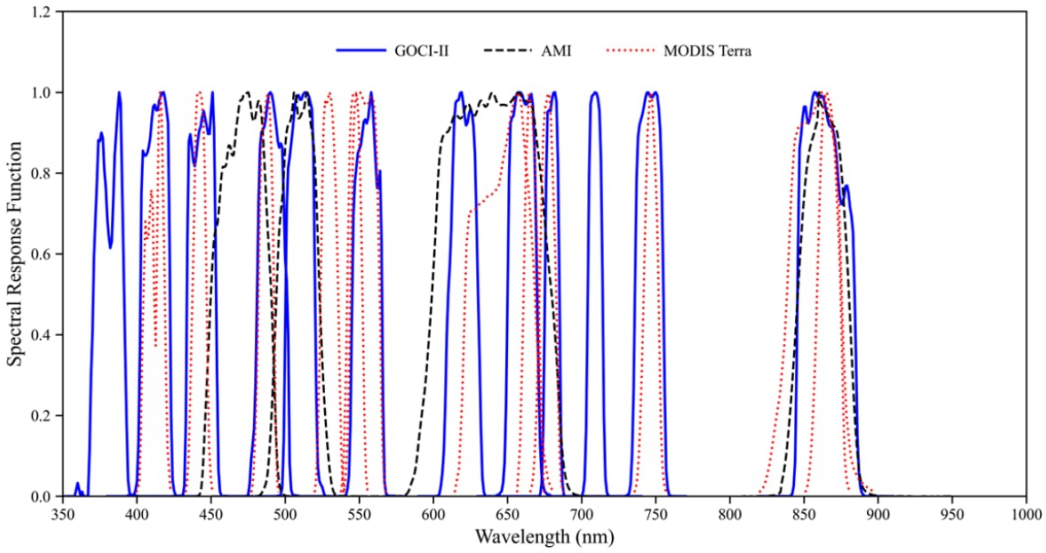


Figure 2. Comparison of the spectral response functions (SRFs) of GOCI-II, AMI, and MODIS Terra, illustrating the spectral correspondence among the sensors used in this study.

2.1.2. Atmospheric and Ancillary Data

The improved atmospheric correction requires radiometric, geometric, atmospheric, and surface ancillary information in addition to the GOCI-II TOA measurements. The datasets used as inputs to the surface reflectance retrieval are summarized in Table 2. GOCI-II L1B TOA radiance (L_TOA) was used as the primary radiometric input, while the GOCI-II coast/land mask was applied to identify land pixels. Pixel-level observation geometry, including sensor azimuth (SenA), sensor zenith (SenZ), solar azimuth (SolA), and solar zenith (SolZ) angles, was obtained from the GOCI-II L2 geometry data. Aerosol optical depth (AOD) was obtained from the GOCI-II L2 AOD product.

Table 2. Input and ancillary datasets used for the GOCI-II atmospheric correction and surface reflectance retrieval.

Input	Source Data	Variables	Provider
TOA radiance	GOCI-II L1B	L_TOA	KHOA/NOSC [1]
Land mask	GOCI-II mask	Coast/land mask	
Observation geometry	GOCI-II L2 geometry	SenA, SenZ, SolA, SolZ	
AOD	GOCI-II L2 AOD	Aerosol optical depth	
Terrain elevation	Copernicus GLO-90 DEM	Elevation	ESA/OpenTopography [2]
Water vapor	GK2A/AMI LE2 TPW	Total precipitable water	KMA/NMSC [3]
Ozone	GK2A AMI LE2 TOZ	Total ozone	

[1] GOCI-II data were obtained from the National Ocean Satellite Center (NOSC), Korea Hydrographic and Oceanographic Agency (KHOA) (https://www.nosc.go.kr/(accessed on 1 October 2026)). [2] The Copernicus GLO-90 DEM was obtained from OpenTopography (https://portal.opentopography.org/ (accessed on 1 October 2026)). [3] GK2A/AMI products were obtained from the National Meteorological Satellite Center (NMSC), Korea Meteorological Administration (KMA) (https://datasvc.nmsc.kma.go.kr/ (accessed on 1 October 2026)).

Terrain elevation was obtained from the Copernicus GLO-90 Digital Elevation Model (DEM). Total precipitable water (TPW) and total ozone (TOZ), representing atmospheric water vapor and ozone conditions, respectively, were obtained from GK2A/AMI Level-2 products. The ancillary datasets were spatially matched to the GOCI-II observation grid before their application to the atmospheric correction procedure.

GOCI-II L1B and L2 products were obtained from the National Ocean Satellite Center (NOSC) of the Korea Hydrographic and Oceanographic Agency (KHOA). The Copernicus GLO-90 DEM was obtained through OpenTopography, and the GK2A/AMI atmospheric products were obtained from the National Meteorological Satellite Center (NMSC) of the Korea Meteorological Administration (KMA). The data providers and access sources are summarized in Table 2.

2.1.3. Reference Datasets for Validation

Independent satellite products were used as reference datasets to evaluate the original and improved GOCI-II land products. Reference datasets were selected according to the physical characteristics of each product and their spectral and temporal compatibility with GOCI-II (Table 3). MODIS MCD19A1 surface reflectance was used for SR validation, MODIS MCD43A3 was used for broadband surface albedo evaluation, and MODIS MOD13Q1 together with GK2A/AMI vegetation indices was used to assess the GOCI-II NDVI and EVI products.

For SR validation, spectrally corresponding GOCI-II and MODIS MCD19A1 bands were selected based on their wavelength characteristics and SRFs (Figure 2). Because the spectral response functions of the two sensors are not identical, comparisons were restricted to bands with appropriate spectral correspondence, and the remaining spectral differences were considered when interpreting the validation results. Figure 2 also shows the spectral characteristics of GK2A/AMI used in the vegetation-index comparison.

Broadband black-sky and white-sky albedo from the GOCI-II LSAB product were evaluated against the corresponding MODIS MCD43A3 products. Direct quantitative validation of the GOCI-II narrowband albedo (LSAN) was not conducted because spectrally equivalent reference bands were not available. For vegetation indices, GOCI-II NDVI and EVI were compared with both GK2A/AMI and MODIS MOD13Q1. The daily GK2A/AMI products were used to examine temporal consistency at a temporal scale comparable to the daily GOCI-II VI products, whereas the 16-day MOD13Q1 composites provided an independent reference for broader spatial and seasonal vegetation patterns.

The validation was conducted using observations from all 12 GOCI-II LA slots (S000–S011) throughout 2023, providing a full-year assessment across the GOCI-II Local Area. The original and improved GOCI-II products were evaluated using the same reference datasets and statistical metrics, while retaining the valid-pixel screening criteria inherent to each product.

Table 3. Summary of the GOCI-II land products and reference datasets used for validation. Both the original and improved products were evaluated using observations from all 12 Local Area slots (S000–S011) throughout 2023.

Product		File Name	Variables	Temporal Resolution	Reference Dataset
Land Surface Reflectance		GK2B_GOCI2_L2_YYYYMMDD_HH_LA_S0##_SRL.nc	12-band surface reflectance; quality flag; latitude and longitude	8 times daily	MODIS MCD19A1
Surface albedo	Broad band	GK2B_GOCI2_L2_YYYYMMDD_HH_LA_S0##_LSAB.nc	1-band black-sky albedo; 1-band white-sky albedo; quality flag; latitude and longitude	Once daily	MODIS MCD43A3
	Narrow band	GK2B_GOCI2_L2_YYYYMMDD_HH_LA_S0##_LSAN.nc	12-band black-sky albedo; 12-band white-sky albedo; quality flag; latitude and longitude	Once daily	Not quantitatively evaluated due to spectral-band differences
Vegetation Index		GK2B_GOCI2_L2_YYYYMMDD_HH_LA_S0##_VI.nc	NDVI; EVI; quality flag; latitude and longitude	Once daily	MODIS MOD13Q1 GK2A AMI

2.2. Overview of the GOCI-II Land Processing Framework

The GOCI-II land processing system consists of a sequential processing chain in which atmospherically corrected surface reflectance serves as the primary input for subsequent land-product retrievals (Figure 3). GOCI-II L1B observations, together with the ancillary atmospheric, geometric, and terrain data described in Section 2.1.2, are first processed through the atmospheric correction module to generate the Level-2 land surface reflectance product (L2 SRL). In the revised processing system, atmospheric correction is performed using a sensor-specific 6SV LUT constructed for the spectral characteristics of the 12 GOCI-II bands. The detailed configuration of the LUT and the revised surface reflectance retrieval procedure are described in the following sections.

The retrieved SR is subsequently processed through the BRDF correction module to generate fixed-viewing BRDF-adjusted reflectance (FVBAR), which serves as an intermediate product in the downstream processing chain. FVBAR is not distributed as a standalone user product but is used internally for the retrieval of surface albedo and vegetation indices. Narrowband black-sky and white-sky albedos are first retrieved for the GOCI-II spectral bands and are subsequently converted to broadband albedo (L2 LSAB). The BRDF-corrected reflectances are also used to derive NDVI and EVI as the L2 vegetation index (VI) product. Thus, changes in the quality of atmospheric correction and SR can propagate through the processing chain and influence the resulting albedo and vegetation-index products.

In this study, the principal algorithmic modification was made at the atmospheric correction and SR retrieval stage. The BRDF correction and vegetation-index formulations were retained from the original processing framework, whereas the narrow-to-broadband conversion coefficients used for broadband albedo retrieval were updated specifically for GOCI-II. Accordingly, changes in the vegetation-index products primarily reflect the propagation of the revised SR through the existing downstream processing chain, whereas changes in

broadband albedo reflect the combined effects of improved SR and the updated narrow-to-broadband conversion. This framework enables the effects of the revised upstream SR retrieval to be assessed at both the reflectance level and the downstream product level, while distinguishing the additional contribution of the updated broadband albedo conversion.

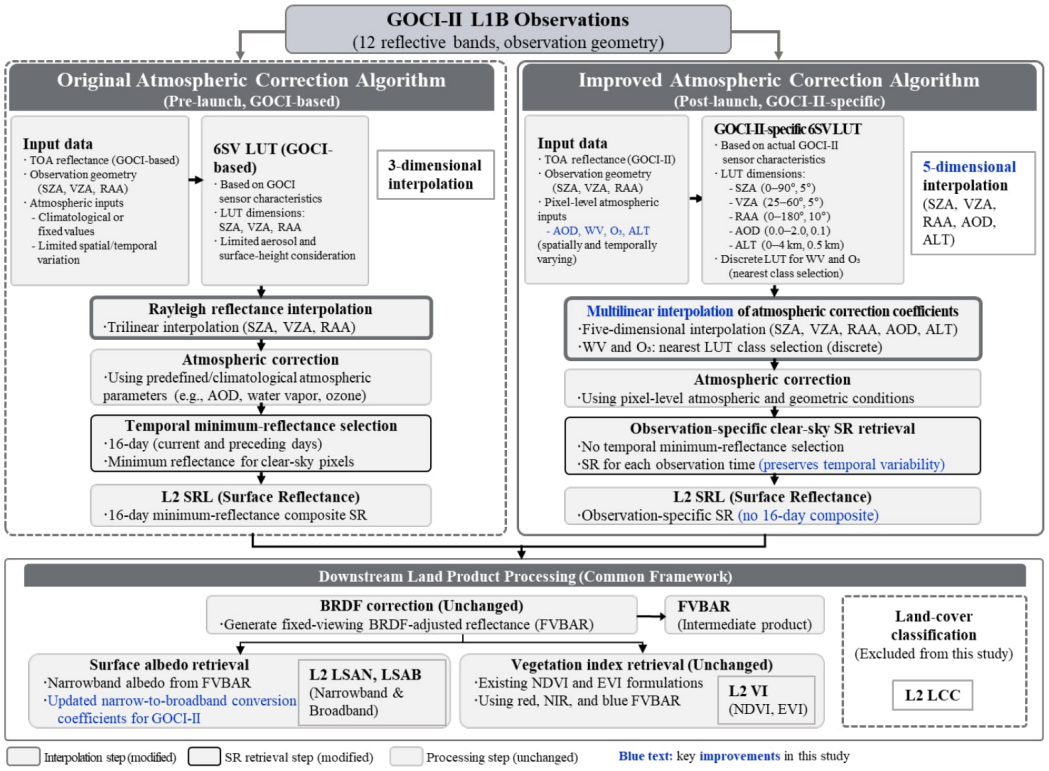


Figure 3. Comparison of the original and improved GOCI-II atmospheric correction algorithms and their integration into the land-product processing framework. The original algorithm employed a 6SV-based atmospheric correction procedure with three-dimensional interpolation of Rayleigh reflectance and temporal minimum-reflectance selection over a 16-day period. The improved algorithm incorporates a GOCI-II-specific 6SV lookup table, five-dimensional interpolation of atmospheric correction coefficients, and pixel-level atmospheric and geometric information to retrieve observation-specific surface reflectance (L2 SRL). The resulting SR is subsequently used in the existing BRDF correction and vegetation-index retrieval procedures, while the narrow-to-broadband conversion coefficients for surface albedo (L2 LSAB) were updated. FVBAR represents an intermediate BRDF-adjusted reflectance product, and land-cover classification (L2 LCC) was excluded from this study.

Accordingly, the original and revised SR, broadband albedo, and vegetation-index products were compared using the validation datasets described in Section 2.1.3. Although the operational GOCI-II processing chain also includes land-cover classification, the land-cover algorithm was newly developed rather than being driven solely by the revised SR input. Therefore, the L2 land-cover classification (LCC) product was excluded from the scope of the present evaluation, as indicated by the gray dashed boxes in Figure 3.

2.3. GOCI-II Surface Reflectance Retrieval

The surface reflectance retrieval constitutes the primary algorithmic modification investigated in this study. The original GOCI-II SR algorithm was developed before launch using proxy observations and combined radiative-transfer-based atmospheric correction with temporal minimum-reflectance compositing. In the revised framework, the atmospheric correction was redesigned specifically for the post-launch GOCI-II sensor using a sensor-specific 6SV LUT and pixel-level atmospheric and geometric information. The fol-

lowing subsections describe the original retrieval approach, the construction of the revised GOCI-II-specific LUT, and its application to individual GOCI-II observations.

2.3.1. Original GOCI-II Surface Reflectance Algorithm

The original GOCI-II surface reflectance algorithm was developed during the pre-launch phase, when operational GOCI-II observations were not yet available. Consequently, GOCI observations were used as proxy input for algorithm development and testing. According to the GOCI-II Surface Reflectance Algorithm Theoretical Basis Document (ATBD) [35], the algorithm was designed as a two-stage processing system consisting of atmospheric correction to generate atmospherically corrected reflectance (ACR), followed by temporal minimum-reflectance selection to produce the final surface reflectance product.

Atmospheric correction in the original algorithm was based on the vector version of the Second Simulation of a Satellite Signal in the Solar Spectrum (6SV). Precomputed LUTs were generated for the 12 GOCI-II spectral bands as functions of solar zenith angle (SZA), viewing zenith angle (VZA), and relative azimuth angle (RAA). The LUT covered SZA from 0° to 80° at 10° intervals, VZA from 0° to 80° at 5° intervals, and RAA from 0° to 180° at 10° intervals. Seasonal atmospheric conditions were represented using standard, midlatitude-summer, and midlatitude-winter atmospheric profiles [35].

For each observation, calibrated GOCI-II Level-1B reflectance and geometric information were used to derive ACR. Rayleigh scattering and gaseous absorption were corrected using the LUT and ancillary atmospheric information. The original ATBD specified OMI products for O_3 and NO_2 and numerical-weather-prediction or climatological information for water vapor when real-time data were unavailable. Aerosol information from Level-2 products was additionally used to identify atmospheric conditions and screen pixels affected by substantial aerosol contamination [35].

The final SR was subsequently determined using a temporal minimum-reflectance approach. This method assumes that surface reflectance remains relatively stable over the compositing interval and that the minimum atmospherically corrected reflectance is less affected by residual atmospheric contamination. Hourly ACR observations were accumulated, and the minimum valid reflectance for each pixel and spectral band was selected from the current observation and observations acquired during the preceding 15 days, resulting in a maximum temporal window of 16 days [35].

However, this approach inherently assumes limited surface change during the compositing period. The original ATBD identifies cloud contamination, land-cover changes, and over- or under-correction of atmospheric effects as potential sources of uncertainty [35]. Moreover, because the final SR is determined through temporal minimum selection, it does not necessarily represent the surface state corresponding to an individual GOCI-II observation time. The original algorithm was also established before actual GOCI-II observations became available and therefore could not fully exploit the post-launch spectral, atmospheric, and geometric information available from the sensor. These characteristics motivated the development of a revised atmospheric correction framework specifically tailored to actual GOCI-II observations, as described in the following section.

2.3.2. Development of the GOCI-II-Specific 6SV LUT

To address the limitations of the original retrieval, the atmospheric correction framework was redesigned specifically for post-launch GOCI-II observations. The major differences between the original and improved SR retrieval frameworks are summarized in Table 4. The revised approach retains 6SV as the radiative transfer model but introduces a GOCI-II-specific multidimensional LUT that explicitly accounts for the atmospheric and geometric conditions of individual observations. In particular, aerosol optical depth (AOD),

water vapor, total column ozone, and terrain elevation were incorporated into the LUT dimensions together with solar and viewing geometry, enabling atmospheric correction to be performed using pixel-level ancillary information.

Table 4. Comparison of the original and improved GOCI-II atmospheric correction and surface reflectance retrieval frameworks.

Component	Original Algorithm	Improved Algorithm
Development basis	Pre-launch GOCI proxy data	Post-launch GOCI-II observations
Radiative Transfer Model	6SV	6SV
Spectral treatment	Pre-launch assumed/ proxy configuration	GOCI-II-specific spectral bands
LUT dimensions	Spectral band + SZA+VZA+RAA+ atmospheric model	Spectral band + SZA+VZA+RAA+elevation+WV+O3+AOD
LUT interpolation method	Trilinear interpolation	Five-dimensional multilinear interpolation
Interpolation variables	SZA, VZA, RAA	SZA, VZA, RAA, ALT, AOD
Interpolation grid points	8 surrounding grid points	32 surrounding grid points
Atmospheric correction coefficients	Interpolation of Rayleigh reflectance LUT with separate gaseous absorption correction	Pixel-specific atmospheric correction coefficients derived from the multidimensional 6SV LUT
Aerosol treatment	L2 aerosol information mainly used for screening	Pixel-level AOD incorporated into LUT-based correction
Atmospheric inputs	Trace-gas ancillary data; climatology when unavailable	Pixel-level AOD, WV, O3 and elevation
Final SR determination	Temporal minimum selection	Observation-specific retrieval
Temporal window	Up to 16 days	Individual observation
Output interpretation	Temporally composited minimum SR	Instantaneous clear-sky SR

The revised LUT was constructed for all 12 GOCI-II bands. Solar zenith angle ranged from 0° to 90° in 5° increments, viewing zenith angle from 25° to 60° in 5° increments, and relative azimuth angle from 0° to 180° in 10° increments. Terrain elevation ranged from 0 to 4 km at 0.5 km intervals. Water vapor ranged from 0 to 5 g cm^{-2} at 1 g cm^{-2} intervals, and total column ozone ranged from 0.25 to 0.35 atm-cm at 0.05 atm-cm intervals. A continental aerosol model was adopted, following previous 6S-based atmospheric correction studies [31,36,37]. In particular, previous sensitivity analyses demonstrated that variations in aerosol optical thickness (AOT) generally had a greater influence on GOCI surface reflectance retrieval than differences among aerosol models [37]. Considering the difficulty of spatially distinguishing aerosol types across East Asia, the continental aerosol model was adopted in the previous GOCI atmospheric correction framework. Following this approach, the present study employed the continental aerosol model, with AOD ranging from 0.0 to 2.0 at intervals of 0.1.

The spectral calculations were performed for GOCI-II Bands 1–12 using their band-specific spectral ranges (Table 5). These parameter combinations resulted in 117,899,712 radiative-transfer cases, producing approximately 1.93 GB of LUT data. The LUT was organized to enable efficient retrieval and interpolation of atmospheric correction coefficients for individual GOCI-II pixels.

Table 5. Parameter ranges and sampling intervals used to construct the GOCI-II-specific 6SV LUT.

LUT Parameters	Range/Model	Interval	No. of Levels
Solar Zenith Angle (°)	0–90	5°	19
View Zenith Angle (°)	25–60	5°	8
Relative Azimuth Angle (°)	0–180	10°	19
Terrain Elevation (km)	0–4	0.5 km	9
Water Vapor (g cm^{-2})	0–5	1 g cm^{-2}	6
Total Column Ozone (atm-cm)	0.25–0.35	0.05 atm-cm	3
Aerosol Model	Continental	-	1
Aerosol Optical Depth (AOD)	0.0–2.0	0.1	21
Spectral Bands	GOCI-II B1-B12 B1: 350–410 nm; B2: 380–440 nm; B3: 410–470 nm; B4: 460–520 nm; B5: 480–540 nm; B6: 520–580 nm; B7: 590–650 nm; B8: 630–690 nm; B9: 650–710 nm; B10: 680–740 nm; B11: 710–770 nm; B12: 820–910 nm;	-	12

A key modification was the extension of the LUT interpolation procedure. The original algorithm employed trilinear interpolation of Rayleigh reflectance using SZA, VZA, and RAA. In contrast, the improved algorithm applies five-dimensional multilinear interpolation using SZA, VZA, RAA, surface altitude (ALT), and AOD. For each pixel, the lower and upper LUT grid points are identified for these five parameters, and normalized interpolation weights are calculated as follows:

$$\omega_j = \frac{x_j - x_{j,L}}{x_{j,U} - x_{j,L}}, j = 1, \ldots, 5 \quad (1)$$

where $x_{j,L}$ and $x_{j,U}$ represent the lower and upper LUT grid values surrounding the actual input x_j, respectively. The interpolated atmospheric correction coefficient C was then calculated as

$$C(x) = \sum_{i_1=0}^{1} \sum_{i_2=0}^{1} \sum_{i_3=0}^{1} \sum_{i_4=0}^{1} \sum_{i_5=0}^{1} C_{i_1 i_2 i_3 i_4 i_5} \prod_{j=1}^{5} \left[\left(1 - i_j\right)\left(1 - \omega_j\right) + i_j \omega_j \right] \quad (2)$$

where $x = (SZA,\ VZA,\ RAA,\ ALT, AOD)$, and $C_{i_1 i_2 i_3 i_4 i_5}$ denotes the atmospheric correction coefficient at each of the 32 surrounding LUT grid points. The interpolation is implemented sequentially along the AOD, ALT, RAA, VZA, and SZA dimensions, reducing the number of intermediate values from 32 to 16, 8, 4, 2, and finally 1. This procedure is applied independently to each atmospheric correction coefficient required for SR retrieval. Water vapor and total column ozone are treated as discrete LUT parameters, with the nearest available LUT classes selected prior to the five-dimensional interpolation. Consequently, the atmospheric correction coefficients vary continuously with observation geometry, surface elevation, and aerosol loading within the LUT parameter ranges.

2.3.3. Atmospheric Correction and Surface Reflectance Retrieval

For each GOCI-II observation, the atmospheric correction was performed using the TOA radiance together with pixel-level solar and viewing geometry, aerosol optical depth, water vapor, ozone, and terrain elevation. These inputs were spatially matched to the GOCI-II grid as described in Section 2.1.2. The corresponding parameter intervals were first identified within the multidimensional LUT, after which the LUT coefficients were interpolated to the atmospheric and geometric state of each individual pixel. The resulting coefficients were then used to invert the TOA signal to surface reflectance. The surface reflectance, ρ_s, was calculated as

$$\rho_S = \frac{aL_{TOA} - b}{1 + c(aL_{TOA} - b)} \quad (3)$$

where L_{TOA} is the GOCI-II TOA radiance and a, b, and c are atmospheric-correction coefficients obtained from the interpolated 6SV LUT for the atmospheric and geometric conditions of each pixel. The coefficients collectively account for the atmospheric path contribution, transmission, and multiple interactions between the atmosphere and surface represented by the radiative-transfer simulations.

A key difference from the original algorithm is that the revised retrieval does not apply temporal minimum-reflectance selection to determine the final SR. Instead, the surface reflectance is retrieved independently for each valid GOCI-II observation using the atmospheric state and observation geometry corresponding to that acquisition. Consequently, the revised SR represents an instantaneous, observation-specific surface reflectance, whereas the original SR represents the minimum reflectance selected from a temporal series extending over as much as 16 days.

Cloud- or otherwise invalid pixels were excluded according to the applicable quality-screening procedure rather than being replaced by temporally composited observations. As a result, the revised product can contain fewer spatially valid pixels than the original temporally composited product, but each retained SR value is explicitly associated with the atmospheric and geometric conditions at the corresponding GOCI-II observation time. This distinction is important for subsequent validation because differences between the original and revised products reflect not only the atmospheric-correction formulation but also the transition from temporally composited SR to observation-specific clear-sky SR.

2.4. Downstream Land Product Retrieval

The effects of the improved surface reflectance retrieval were further evaluated for downstream GOCI-II land products, including surface albedo and vegetation indices. In the operational GOCI-II land processing chain, atmospherically corrected surface reflectance is first used for BRDF modeling, from which fixed-viewing BRDF-adjusted reflectance (FVBAR) and BRDF parameters are derived. These intermediate products are subsequently used to retrieve narrowband albedo and vegetation indices, while broadband albedo is obtained through narrow-to-broadband conversion [33]. The BRDF modeling and vegetation-index formulations were retained from the original GOCI-II processing framework [33]. However, the narrow-to-broadband conversion coefficients used for broadband albedo retrieval were recalculated in this study to reflect the spectral characteristics of GOCI-II. The original conversion coefficients had been developed using GOCI spectral bands, whereas the revised coefficients were derived using GOCI-II narrowband albedo and MODIS MCD43A3 broadband albedo data from 2023.

2.4.1. BRDF Adjustment and FVBAR

GOCI-II surface reflectance was adjusted for directional reflectance effects using the semi-empirical Roujean BRDF model [33]. Because GOCI-II is not a multi-angle sensor,

observations acquired over a temporal window are combined to provide the angular variability required for BRDF modeling. The original algorithm uses a 16-day synthesis period, with BRDF parameters from previous days used for gap filling when valid observations are unavailable because of persistent cloud contamination [33].

The Roujean model represents surface reflectance using isotropic, geometric, and volumetric scattering components [33]. In the GOCI-II implementation, the viewing geometry of each pixel is retained during reflectance normalization to account for the fixed-viewing characteristics of geostationary observations. The resulting normalized reflectance is referred to as fixed-viewing BRDF-adjusted reflectance (FVBAR), which is an intermediate product used for subsequent albedo and vegetation-index retrievals [33]. The BRDF parameters and FVBAR are generated internally and are not distributed as standalone Level-2 products.

2.4.2. Surface Albedo Retrieval and Narrow-to-Broadband Conversion

Surface albedo was retrieved from the BRDF parameters following the original GOCI-II albedo framework [33]. Black-sky albedo (BSA) and white-sky albedo (WSA) represent the limiting cases of completely direct and completely diffuse illumination, respectively. For each GOCI-II spectral band, the BRDF kernel functions were integrated over the relevant illumination and viewing geometries, and the resulting hemispherical kernel integrals were combined with the BRDF parameters to derive narrowband BSA and WSA [33]. The 12-band narrowband albedo products constitute the GOCI-II L2 LSAN product.

For applications requiring total shortwave surface albedo, the narrowband albedos were subsequently converted to broadband albedo using a linear narrow-to-broadband transformation. The original GOCI-II processing framework adopts a regression-based conversion in which broadband albedo is expressed as a linear combination of the sensor-specific narrowband albedos [33]. However, the conversion coefficients originally implemented in the processing chain were based on spectral characteristics available during the pre-launch algorithm-development phase. Therefore, new narrow-to-broadband conversion coefficients were derived in this study using actual GOCI-II narrowband albedo observations.

The new coefficients were derived using daily GOCI-II L2 LSAN and MODIS MCD43A3 products acquired in 2023. GOCI-II LSAN provides BSA and WSA for 12 spectral bands centered at 380, 412, 443, 490, 510, 555, 620, 660, 680, 709, 745, and 865 nm. Nine GOCI-II Local Area slots containing substantial land areas (S001, S002, S004, S005, S007, S008, S009, S010, and S011) were used, together with nine spatially corresponding MODIS MCD43A3 tiles. The datasets covered the period from 16 January to 31 December 2023. A total of approximately 222 GOCI-II images were used to derive the narrow-to-broadband albedo conversion coefficients, while a separate dataset of approximately 96 GOCI-II images was reserved for accuracy validation. The two datasets were mutually exclusive, with no overlap between the images used for coefficient estimation and validation.

Prior to regression analysis, the GOCI-II and MODIS products were reprojected to a common geographic reference system and resampled to a spatial resolution of 1 km. The GOCI-II slots and MODIS tiles were mosaicked separately for each date, and the MODIS mosaics were subset to the spatial extent of the corresponding GOCI-II data. Only pixels containing valid finite values in both the reference broadband albedo and all 12 GOCI-II narrowband albedo bands were retained for coefficient estimation.

The GOCI-II-specific broadband albedo was estimated using an intercept-inclusive multiple linear regression:

$$\mathbf{A_{BB}} = \boldsymbol{\omega}_0 + \sum_{\mathbf{i}=1}^{12} \boldsymbol{\omega}_\mathbf{i}\boldsymbol{\alpha}_\mathbf{i} = \boldsymbol{\omega}_0 + \boldsymbol{\omega}_1\boldsymbol{\alpha}_1 + \boldsymbol{\omega}_2\boldsymbol{\alpha}_2 + \ldots + \boldsymbol{\omega}_{12}\boldsymbol{\alpha}_{12}, \quad (4)$$

where A_{BB} represents shortwave broadband albedo, α_i is the GOCI-II narrowband albedo for band i, and ω_0 and ω_i are the intercept and band-specific conversion coefficients, respectively.

MODIS MCD43A3 shortwave BSA or WSA was used as the dependent variable, whereas the 12 corresponding GOCI-II narrowband albedos were used as independent variables. Separate regression models were developed for BSA and WSA.

To accommodate the large volume of image data, the regression statistics were accumulated sequentially over 512 × 512-pixel processing windows rather than loading the complete annual dataset simultaneously. Only valid pixels were retained, and up to 5000 valid pixels were randomly sampled from each window to maintain spatial representativeness while reducing computational requirements. Regression coefficients were estimated from the accumulated samples over the entire 2023 dataset rather than separately for individual dates.

The resulting GOCI-II-specific narrow-to-broadband conversion coefficients are listed in Table 6. Separate coefficient sets were obtained for BSA and WSA. The resulting daily broadband BSA and WSA constitute the GOCI-II L2 LSAB product. Unlike the broadband albedo retrieval, for which the narrow-to-broadband conversion coefficients were updated in this study, the formulations used for the vegetation indices were retained from the original GOCI-II algorithm [33], as described in Section 2.4.3.

Table 6. GOCI-II-specific narrow-to-broadband conversion coefficients for black-sky and white-sky albedo.

Coefficient	Black-Sky Albedo	White-Sky Albedo
ω_0	0.108139077	0.068727224
ω_1	−0.000220764	0.000000542
ω_2	−0.029121721	−0.06045334
ω_3	−0.101903884	−0.144199271
ω_4	0.124697087	0.030734721
ω_5	−0.021760481	−0.008438298
ω_6	−0.065842125	−0.252569843
ω_7	−0.222830472	−0.300815524
ω_8	0.354594367	0.352951648
ω_9	0.013678175	0.581643372
ω_{10}	−0.021547482	−0.135955962
ω_{11}	0.043663598	0.260271294
ω_{12}	0.020186703	0.047552699

2.4.3. Vegetation Index Retrieval

Vegetation indices were calculated from FVBAR rather than directly from instantaneous surface reflectance, thereby reducing variations associated with illumination and viewing geometry [33]. NDVI was calculated using the red and near-infrared FVBAR:

$$NDVI = \frac{\rho_{NIR} - \rho_{Red}}{\rho_{NIR} + \rho_{Red}}, \quad (5)$$

where ρ_{NIR} and ρ_{Red} are FVBAR in the near-infrared and red bands, respectively [33].

EVI additionally incorporates the blue-band FVBAR to reduce the effects of atmospheric contamination and canopy background [33]:

$$EVI = G\frac{\rho_{NIR} - \rho_{Red}}{\rho_{NIR} + C_1\rho_{Red} - C_2\rho_{Blue} + L}, \quad (6)$$

where ρ_{Blue} is the blue-band FVBAR, and G, C_1, C_2, and L are the gain, aerosol-resistance, and canopy-background adjustment coefficients defined in the original algorithm [33]. The NDVI and EVI formulations themselves were not modified in this study; therefore, differences between the original and improved vegetation-index products primarily reflect changes propagated from the upstream SR retrieval.

NDVI and EVI were retained as the operational vegetation-index products defined in the original GOCI-II land-product framework [33]. Since the objective of this study was to evaluate the effects of the revised SR processing framework on existing downstream products, the original vegetation-index formulations were maintained without modification. This approach enables a consistent assessment of changes in vegetation-index accuracy without introducing additional differences arising from alternative index formulations.

2.5. Validation Strategy and Accuracy Metrics

The original and improved GOCI-II land products were quantitatively evaluated using independent satellite products over the 2023 study period. The validation was designed to assess not only the accuracy of the revised surface reflectance retrieval itself, but also the extent to which changes in the upstream SR product were propagated to downstream surface albedo and vegetation-index products. For each product, GOCI-II observations were spatially matched with the corresponding reference datasets described in Section 2.1.3, and only valid pixels available for comparison were included in the statistical analysis. For the primary validation, the original and improved products were evaluated using the valid pixels retained by their respective processing schemes, thereby representing the performance of each product under its operational configuration. Because differences in valid-pixel screening may affect the resulting validation statistics, an additional common-pixel analysis was performed using only observations for which the original product, improved product, and reference dataset were simultaneously valid. This supplementary analysis was used to distinguish changes attributable to the retrieval algorithm from those associated with differences in sample availability.

For surface reflectance validation, GOCI-II SR was compared with the MODIS MCD19A1 surface reflectance product. Six spectrally corresponding bands were selected for quantitative comparison: GOCI-II bands centered at 412, 443, 490, 555, 660, and 865 nm and the corresponding MODIS bands centered at approximately 412.5, 443, 488, 551, 645, and 858.5 nm, respectively. The original and improved GOCI-II SR products were evaluated separately against MODIS using all valid matched observations in 2023. Band-wise scatterplots and statistical measures were used to characterize systematic bias, dispersion, linear association, and overall retrieval error. The number of valid samples was also reported because cloud and quality screening in the improved retrieval substantially reduced the number of retained observations relative to the original temporally composited SR product.

Broadband surface albedo was evaluated against MODIS MCD43A3. Daily black-sky albedo (BSA) and white-sky albedo (WSA) from the original and improved GOCI-II LSAB products were independently compared with the corresponding MODIS broadband albedo. The comparison was performed over the full year of 2023, and monthly statistics were additionally calculated to examine seasonal variations in retrieval performance. This monthly assessment was included because aerosol conditions, vegetation state, snow cover, and solar illumination geometry vary substantially throughout the year and may affect albedo retrieval accuracy. The evaluation therefore considered both annual-scale agreement and month-to-month behavior in bias and RMSE.

Vegetation-index validation was conducted for both NDVI and EVI using two independent reference datasets. Daily GOCI-II VI products were compared with daily GK2A/AMI vegetation indices to assess temporal consistency at a comparable temporal resolution. MODIS MOD13Q1 was additionally used as an independent reference for spatial and seasonal vegetation patterns; because MOD13Q1 is a 16-day composite product, it was not interpreted as a direct daily reference in the same manner as AMI. For quantitative comparisons, the satellite datasets were spatially aligned to the coarser-resolution grid using nearest-neighbor resampling. Temporal matching with MODIS MOD13Q1 was per-

formed using the last day of each 16-day compositing period as the reference date, whereas GK2A/AMI observations were matched to the corresponding GOCI-II acquisition times. In addition to these matched comparisons, the original vegetation-index time series from each satellite product were analyzed separately to examine seasonal variations without imposing identical temporal sampling. Spatial distributions and temporal profiles were examined together with quantitative pixel-wise comparisons. The original and improved GOCI-II NDVI and EVI products were evaluated separately against both reference datasets to determine whether the revised upstream processing resulted in improved agreement with independent satellite observations. Quantitative comparisons of both NDVI and EVI were based on valid matched pixels and included sample size, bias, correlation coefficient, and RMSE.

The quantitative performance of all products was assessed using the number of valid samples (N), mean bias, Pearson correlation coefficient (r), and root mean square error (RMSE). Bias was calculated as

$$Bias = \frac{1}{N}\sum_{i=1}^{N}(G_i - R_i), \tag{7}$$

where G_i and R_i denote the GOCI-II estimate and corresponding reference value for pixel i, respectively. Positive bias therefore indicates an overall overestimation by GOCI-II, whereas negative bias indicates underestimation.

The Pearson correlation coefficient was calculated as

$$r = \frac{\sum_{i=1}^{N}\left(G_i - \overline{G}\right)\left(R_i - \overline{R}\right)}{\sqrt{\sum_{i=1}^{N}\left(G_i - \overline{G}\right)^2}\sqrt{\sum_{i=1}^{N}\left(R_i - \overline{R}\right)^2}}, \tag{8}$$

where $\overline{G}$ and $\overline{R}$ denote the mean values of the GOCI-II estimates and reference data, respectively. RMSE was calculated as

$$RMSE = \sqrt{\frac{1}{N}\sum_{i=1}^{N}(G_i - R_i)^2}. \tag{9}$$

Together, these metrics characterize complementary aspects of retrieval performance: bias represents systematic deviation, *r*describes the consistency of spatial and temporal variations between datasets, and RMSE quantifies the overall magnitude of the differences. The same set of metrics was applied to the original and improved products to provide a consistent basis for evaluating changes in product performance.

3. Results

3.1. Surface Reflectance

The improved GOCI-II surface reflectance (SR) product provided spatially continuous observations of land-surface reflectance throughout the daytime observation period. Figure 4 shows hourly natural-color composites from 00:00 to 08:00 UTC on 9 May 2023. Although the spatial extent of valid observations varied among acquisition times because only clear-sky pixels retained after cloud screening were displayed, consistent land-surface patterns were observed across successive hourly acquisitions.

The spectral characteristics of the original and improved SR products were further examined over representative vegetation, bare soil, and urban surfaces (Figure 5). Distinct differences were observed between the original and improved GOCI-II spectra, particularly at shorter wavelengths. For vegetation, the original product exhibited substantially higher reflectance in the visible bands than both the improved product and MODIS MCD19A1, whereas the improved product showed lower visible reflectance and a more pronounced

contrast between the visible and near-infrared regions. For bare soil and urban surfaces, the improved product also exhibited spectral patterns that were generally closer to those of MODIS, particularly across the visible wavelengths. Differences remained in the near-infrared region, indicating that the degree of agreement varied with both wavelength and surface type.

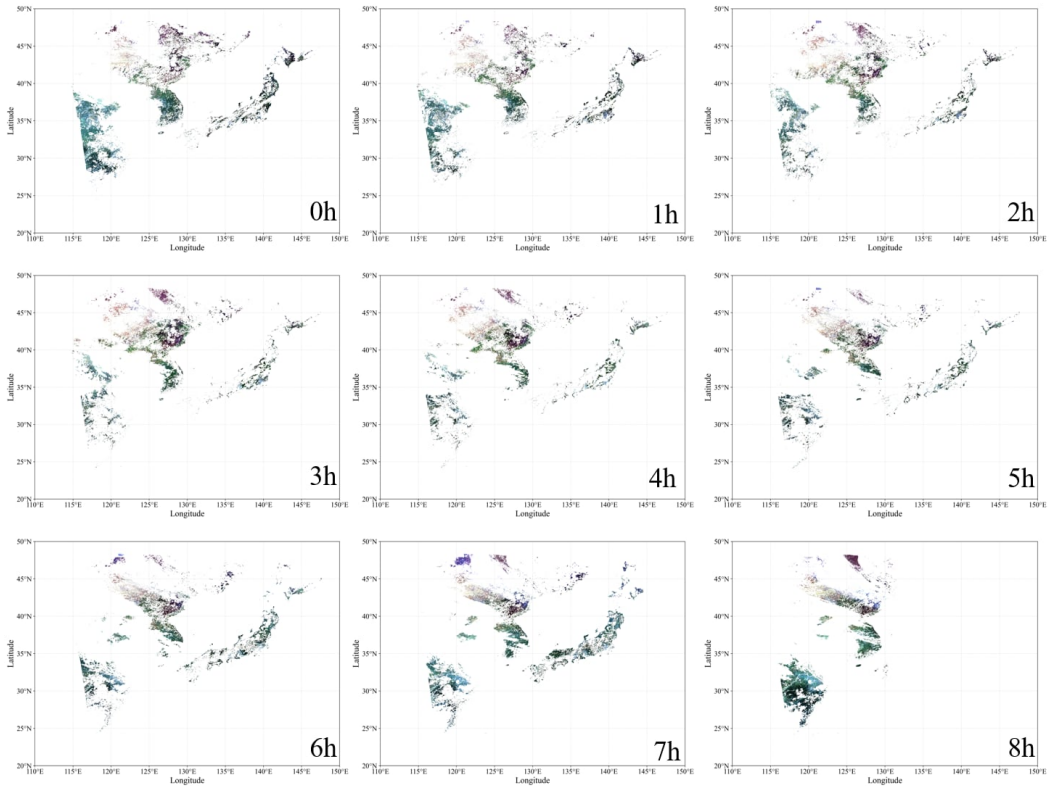


Figure 4. Hourly natural-color composites of the improved GOCI-II surface reflectance (SR) product from 00:00 to 08:00 UTC on 9 May 2023. Only valid clear-sky pixels retained after cloud screening are displayed.

Quantitative validation against MODIS MCD19A1 confirmed substantial differences between the original and improved SR products (Figure 6 and Table 7). Six spectrally corresponding GOCI-II bands centered at 412, 443, 490, 555, 660, and 865 nm were evaluated against the corresponding MODIS bands. The largest improvements occurred at shorter wavelengths. Bias decreased from 0.212, 0.154, and 0.098 in the original product to 0.018, 0.006, and 0.018 in the improved product at 412, 443, and 490 nm, respectively. Correspondingly, RMSE decreased from 0.271 to 0.042, from 0.196 to 0.032, and from 0.134 to 0.036. Improvements were also observed at longer wavelengths. At 555 and 660 nm, RMSE decreased from 0.092 and 0.080 to 0.034 and 0.037, respectively, while at 865 nm, bias changed from −0.130 to 0.012 and RMSE decreased from 0.162 to 0.075.

Changes in correlation were less uniform than those in bias and RMSE. For the full set of valid pixels, r decreased slightly from 0.550 to 0.511 at 412 nm and from 0.582 to 0.576 at 443 nm, whereas it increased from 0.621 to 0.701 at 490 nm, from 0.604 to 0.703 at 555 nm, from 0.699 to 0.841 at 660 nm, and from 0.458 to 0.624 at 865 nm (Table 7). Overall, the improved product exhibited substantially lower systematic and absolute differences from MCD19A1 across all six evaluated bands, with the largest reductions in bias and RMSE occurring at shorter wavelengths.

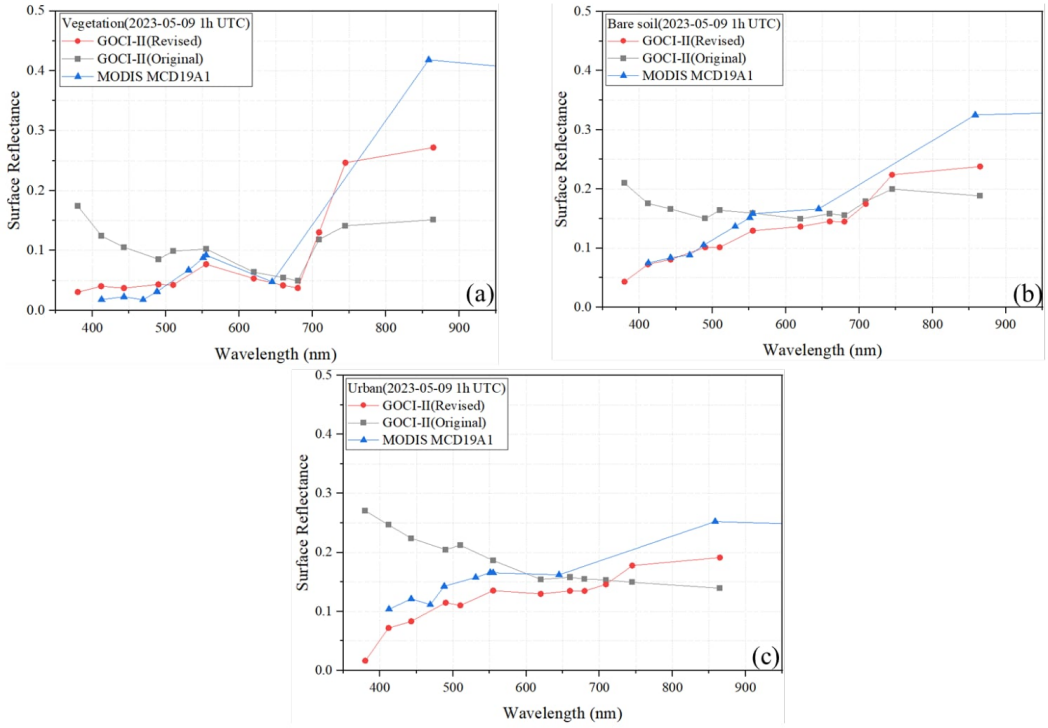


Figure 5. Comparison of surface reflectance spectra from the original and improved GOCI-II products and MODIS MCD19A1 over representative (**a**) vegetation, (**b**) bare soil, and (**c**) urban areas at 01:00 UTC on 9 May 2023.

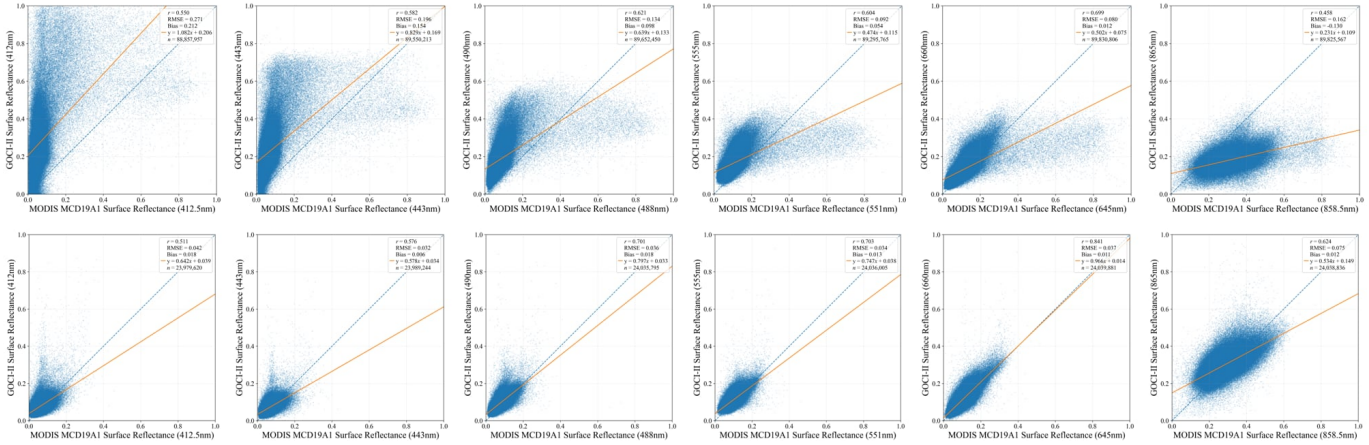


Figure 6. Comparison of the original (**top row**) and improved (**bottom row**) GOCI-II surface reflectance (SR) against MODIS MCD19A1 surface reflectance for six spectrally corresponding bands in 2023. From left to right, the GOCI-II bands centered at 412, 443, 490, 555, 660, and 865 nm are compared with the corresponding MODIS bands centered at 412.5, 443, 488, 551, 645, and 858.5 nm, respectively. The dashed lines indicate the 1:1 relationship, and the solid lines represent linear regression fits.

The number of valid pixel pairs, however, differed considerably between the two products. Approximately 89 million valid pairs per band were available for the original product, whereas approximately 24 million were retained for the improved product (Table 7). To examine whether the observed accuracy differences were associated with this difference in sample availability, an additional validation was performed using only pixels that were simultaneously valid in the original GOCI-II, improved GOCI-II, and MODIS MCD19A1 products (Table 8). The slight differences in valid-pixel counts between Tables 7 and 8 resulted from an additional resampling step in which the improved GOCI-II SR data, previously resampled to the MODIS grid, were realigned to the original GOCI-II grid. The

same common valid-pixel mask was then applied to both the original and improved GOCI-II SR datasets to ensure a consistent basis for comparison.

Table 7. Validation statistics of the original and improved GOCI-II surface reflectance against MODIS MCD19A1 for six spectrally corresponding bands in 2023.

GOCI-II Band (nm)	MODIS Band (nm)	Version	N	Bias	*r*	RMSE
412	412.5	Original	88,857,957	0.212	0.550	0.271
		Improved	23,979,620	0.018	0.511	0.042
443	443	Original	89,550,213	0.154	0.582	0.196
		Improved	23,989,244	0.006	0.576	0.032
490	488	Original	89,652,450	0.098	0.621	0.134
		Improved	24,035,795	0.018	0.701	0.036
555	551	Original	89,295,765	0.054	0.604	0.092
		Improved	24,036,005	0.013	0.703	0.034
660	645	Original	89,830,806	0.012	0.699	0.080
		Improved	24,039,881	0.011	0.841	0.037
865	858.5	Original	89,825,567	−0.130	0.458	0.162
		Improved	24,038,836	0.012	0.624	0.075

Table 8. Validation statistics of the original and improved GOCI-II surface reflectance against MODIS MCD19A1 using common valid pixels in 2023.

GOCI-II Band (nm)	MODIS Band (nm)	N	Version	Bias	*r*	RMSE
412	412.5	23,986,262	Original	0.203	0.494	0.244
			Improved	0.018	0.512	0.042
443	443	24,013,115	Original	0.158	0.605	0.183
			Improved	0.006	0.579	0.032
490	488	24,059,579	Original	0.110	0.722	0.126
			Improved	0.018	0.705	0.036
555	551	24,059,542	Original	0.070	0.699	0.083
			Improved	0.013	0.708	0.034
660	645	24,062,082	Original	0.030	0.840	0.048
			Improved	0.011	0.846	0.036
865	858.5	24,061,627	Original	−0.119	0.479	0.144
			Improved	0.012	0.634	0.074

Under this common-pixel condition, the reductions in bias and RMSE were consistently maintained. At 412, 443, and 490 nm, RMSE decreased from 0.244, 0.183, and 0.126 in the original product to 0.042, 0.032, and 0.036 in the improved product, respectively. At 555, 660, and 865 nm, RMSE decreased from 0.083, 0.048, and 0.144 to 0.034, 0.036, and 0.074, respectively. Bias was also substantially reduced, particularly at 412, 443, 490, and 865 nm. Correlation showed smaller and band-dependent changes: r increased at 412, 555, 660, and 865 nm, whereas slight decreases were observed at 443 and 490 nm (Table 8). These results show that the substantial reductions in bias and RMSE persisted when the original and improved products were evaluated using an identical set of valid pixels.

3.2. Surface Albedo

The effects of the revised processing were subsequently examined for the downstream surface albedo products. Figure 7 compares natural-color composites generated from the narrowband surface albedo (LSAN) for the original and improved GOCI-II products, with MODIS MCD43A3 included for qualitative comparison. Both black-sky albedo (BSA) and white-sky albedo (WSA) exhibited noticeable changes in their spatial and spectral appearance after improvement. The improved LSAN composites showed substantially different surface patterns from the original product, demonstrating that changes introduced in the upstream SR retrieval propagated into the narrowband albedo product.

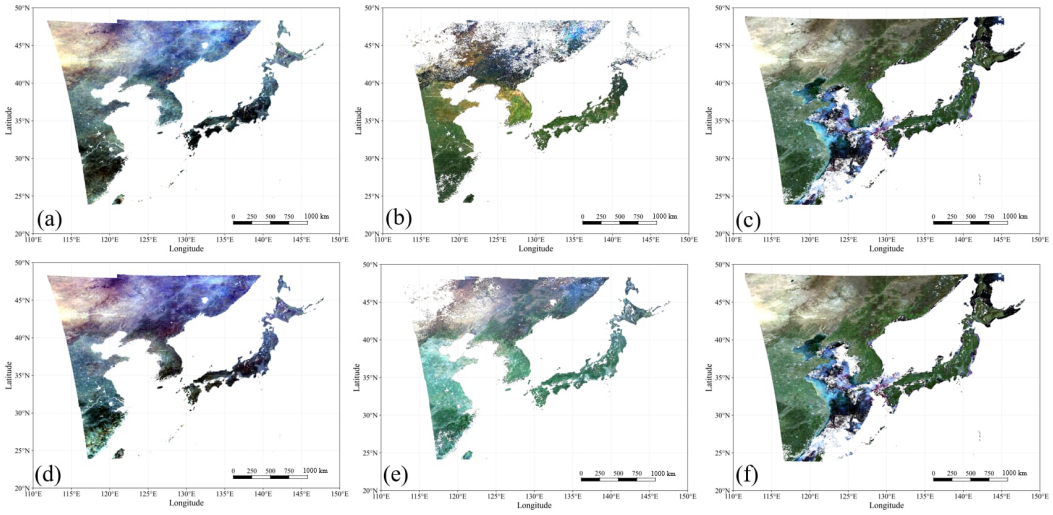


Figure 7. Natural-color composites of narrowband surface albedo (LSAN) on 9 May 2023 from the original GOCI-II product [(**a**) BSA and (**d**) WSA], the improved GOCI-II product [(**b**) BSA and (**e**) WSA], and MODIS MCD43A3 [(**c**) BSA and (**f**) WSA], shown for qualitative comparison of spatial patterns.

The corresponding broadband albedo (LSAB) products are shown in Figure 8. Spatial differences between the original and improved GOCI-II products were apparent for both BSA and WSA, and the improved products exhibited distributions that were generally more consistent with the spatial patterns observed in MODIS MCD43A3. The accuracy of the retrieved broadband albedo was evaluated using an independent dataset of approximately 96 GOCI-II images that were not used to derive the narrow-to-broadband conversion coefficients.

The annual validation statistics further demonstrated the changes in broadband albedo performance (Table 9). For BSA, bias decreased in magnitude from −0.011 to −0.001, while RMSE decreased from 0.037 to 0.025. The correlation coefficient increased slightly from 0.397 to 0.411. For WSA, bias decreased in magnitude from −0.013 to −0.002 and RMSE decreased from 0.039 to 0.035, while the correlation coefficient increased more substantially from 0.395 to 0.581.

Table 9. Validation statistics of the original and improved GOCI-II broadband surface albedo against MODIS MCD43A3 in 2023.

Albedo Type	Product	N	Bias	*r*	RMSE
Black-sky	Original	118,816,465	−0.011	0.397	0.037
	Improved	46,221,586	−0.001	0.411	0.025
White-sky	Original	118,608,143	−0.013	0.395	0.039
	Improved	82,632,608	−0.002	0.581	0.035

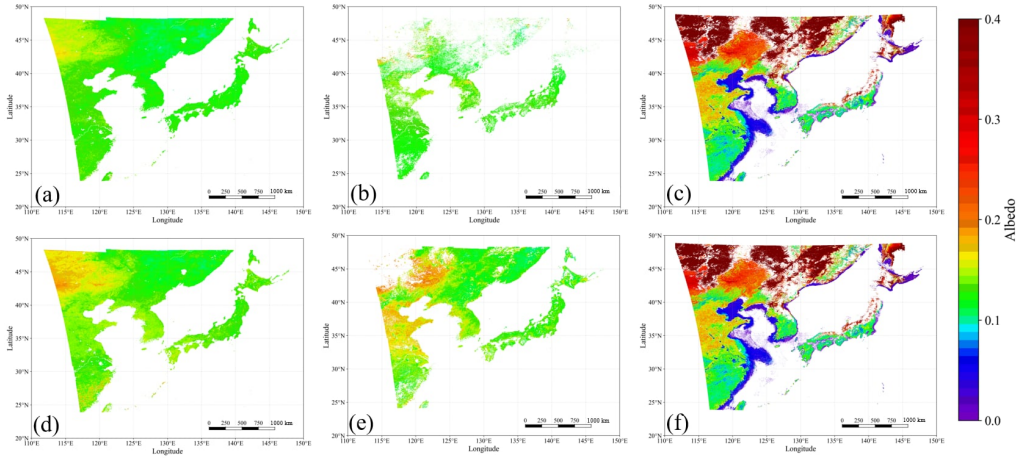


Figure 8. Spatial comparison of daily broadband surface albedo (LSAB) from the original and improved GOCI-II products and MODIS MCD43A3 on 9 May 2023. The upper panels show BSA from (**a**) original GOCI-II, (**b**) improved GOCI-II, and (**c**) MODIS MCD43A3, while the lower panels show WSA from (**d**) original GOCI-II, (**e**) improved GOCI-II, and (**f**) MODIS MCD43A3.

The monthly validation results showed that the magnitude of improvement varied throughout the year (Figure 9). For BSA, the improved product generally exhibited bias values closer to zero and lower RMSE than the original product throughout most months. The reduction in negative bias was particularly apparent from spring through autumn. For WSA, the improved product likewise showed smaller absolute bias and lower RMSE during most of the year. However, an exception occurred in November, when the RMSE of the improved WSA increased markedly relative to both the other months and the original product. Thus, although the annual statistics indicate an overall improvement in broadband albedo, the magnitude and consistency of the improvement differed between BSA and WSA and among seasons.

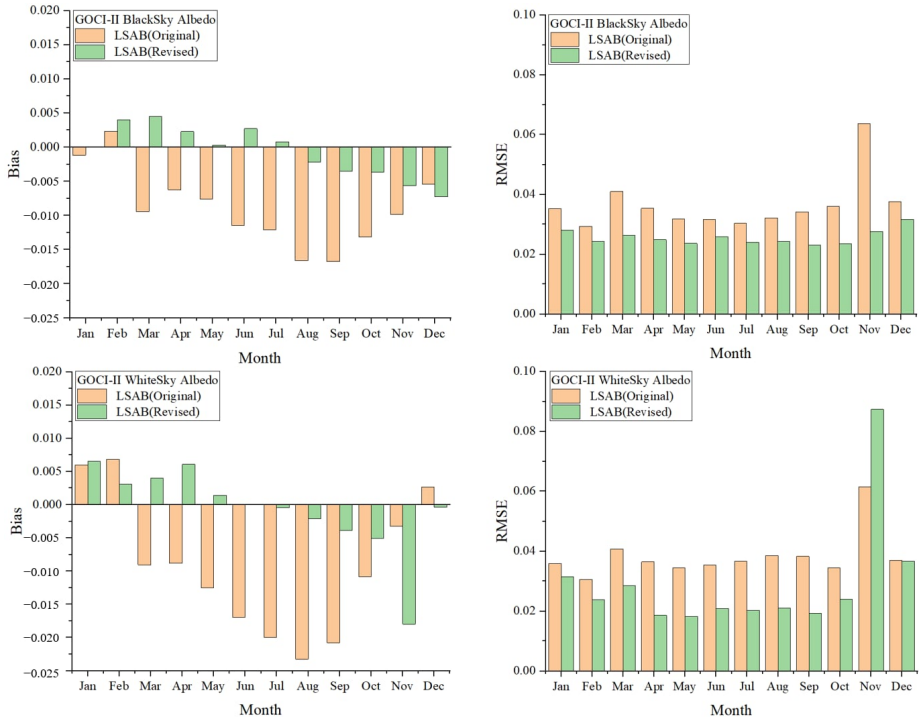


Figure 9. Monthly validation results of the original and improved GOCI-II broadband surface albedo against MODIS MCD43A3 in 2023: bias and RMSE for black-sky albedo (**top panels**) and white-sky albedo (**bottom panels**).

3.3. Vegetation Indices

The influence of the revised processing was also evident in the vegetation-index products. Figure 10 compares the spatial distributions of NDVI and EVI from the original and improved GOCI-II products with those from GK2A/AMI and MODIS MOD13Q1. The original GOCI-II NDVI exhibited systematically lower values over extensive vegetated regions, whereas the improved NDVI showed higher values and spatial patterns that were more consistent with the reference satellite products. A similar change was observed for EVI, although the magnitude of the spatial differences varied among the products.

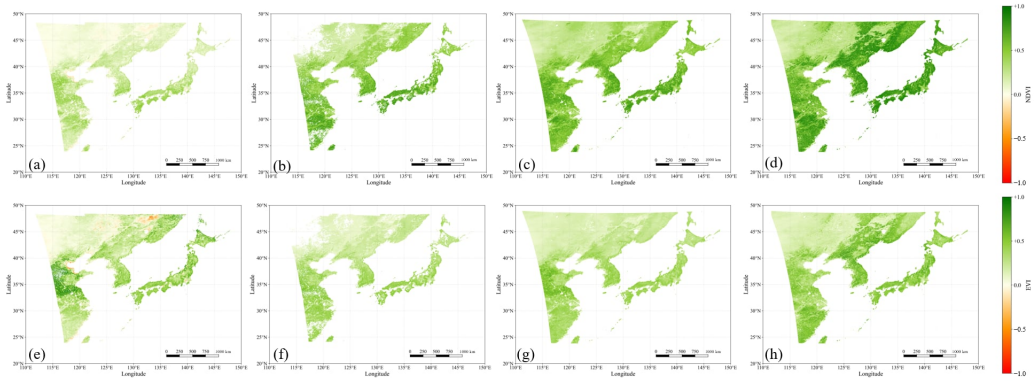


Figure 10. Spatial comparison of vegetation indices from the original and improved GOCI-II products and reference satellite products. The upper panels show NDVI from (**a**) original GOCI-II, (**b**) improved GOCI-II, (**c**) GK2A/AMI at 01:00 UTC on 9 May 2023, and (**d**) the corresponding MODIS MOD13Q1 16-day composite. The lower panels (**e**–**h**) show the corresponding EVI products in the same order.

The temporal behavior of the vegetation indices was examined over a representative vegetated area throughout 2023 (Figure 11). The improved GOCI-II NDVI reproduced the seasonal increase during the growing season and subsequent decrease toward the end of the year more clearly than the original product. Its seasonal trajectory was also more consistent with the variations observed in GK2A/AMI and MODIS MOD13Q1. A similar seasonal pattern was observed for EVI. The comparison additionally illustrates the difference in temporal sampling between the daily GOCI-II and GK2A/AMI products and the 16-day composite MODIS MOD13Q1 product.

Quantitative validation showed substantial improvements for both vegetation indices (Table 10). Against MODIS MOD13Q1, NDVI bias decreased in magnitude from −0.367 to −0.060 and RMSE decreased from 0.403 to 0.142, while *r*increased from 0.774 to 0.841. Against GK2A/AMI, NDVI bias decreased from −0.321 to −0.011 and RMSE from 0.342 to 0.100, accompanied by an increase in *r*from 0.828 to 0.891.

The improvement was also evident for EVI. Relative to MODIS MOD13Q1, bias changed from −0.091 to 0.013, RMSE decreased from 0.274 to 0.111, and *r*increased from 0.577 to 0.789. Relative to GK2A/AMI, bias was reduced from −0.103 to −0.001, RMSE decreased from 0.268 to 0.071, and *r*increased markedly from 0.650 to 0.902. Overall, both NDVI and EVI showed reduced systematic differences and RMSE after improvement, together with increased correlations with the two independent reference products.

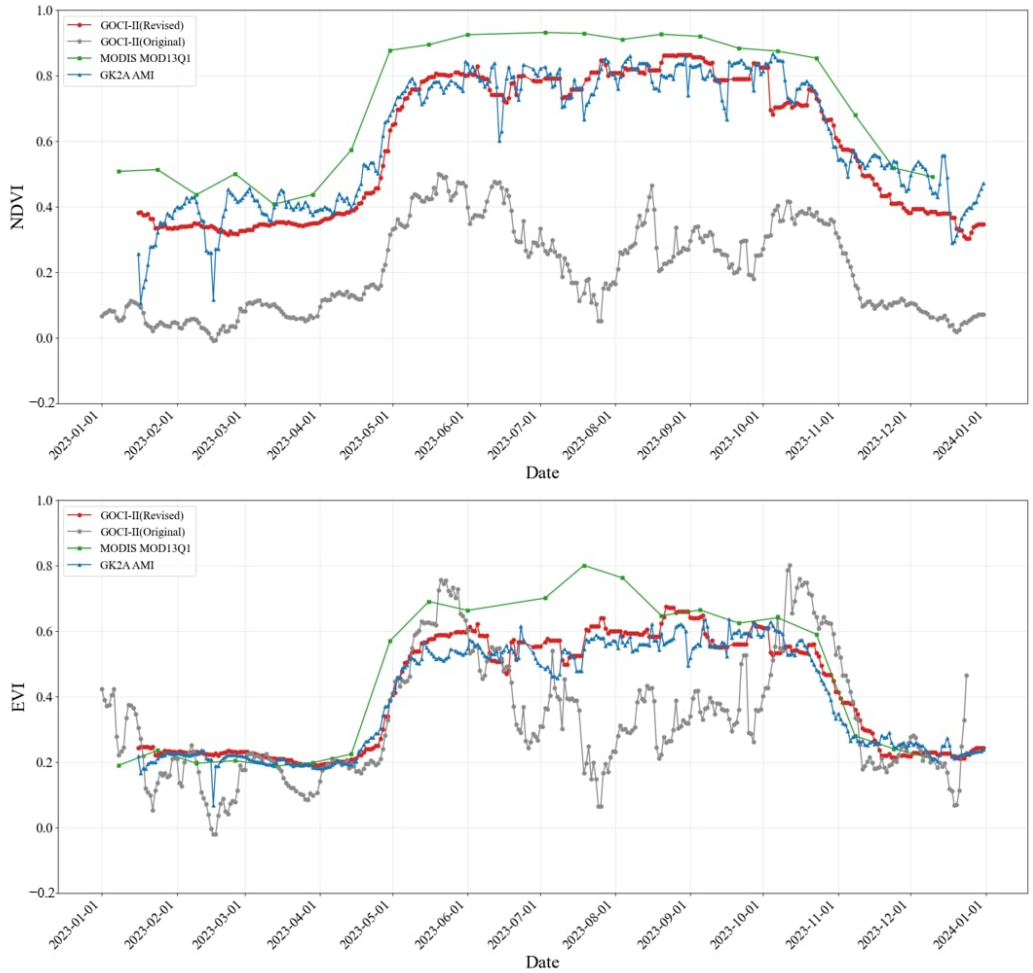


Figure 11. Temporal variations in NDVI (**top**) and EVI (**bottom**) over a representative vegetated area in 2023, comparing daily original and improved GOCI-II products with daily GK2A/AMI and 16-day composite MODIS MOD13Q1 products.

Table 10. Validation statistics of the original and improved GOCI-II vegetation indices against MODIS MOD13Q1 and GK2A/AMI in 2023.

VI	Reference	Product	N	Bias	*r*	RMSE
NDVI	MOD13Q1	Original	8,961,746	−0.367	0.774	0.403
		Improved	5,670,762	−0.060	0.841	0.142
	AMI	Original	8,937,979	−0.321	0.828	0.342
		Improved	5,620,980	−0.011	0.891	0.100
EVI	MOD13Q1	Original	7,589,369	−0.091	0.577	0.274
		Improved	5,624,776	0.013	0.789	0.111
	AMI	Original	7,571,439	−0.103	0.650	0.268
		Improved	5,617,778	−0.001	0.902	0.071

4. Discussion

4.1. Improvement of GOCI-II Surface Reflectance Through Sensor-Specific Atmospheric Correction

The revised atmospheric correction substantially reduced systematic and overall errors in GOCI-II surface reflectance, with the most pronounced improvements occurring at shorter wavelengths. The original product exhibited strong positive biases at 412–490 nm, whereas these biases were markedly reduced after application of the revised algorithm. This spectral dependence is consistent with the stronger influence of molecular scattering and

aerosols at shorter wavelengths, where accurate characterization of atmospheric conditions is particularly important. The improved performance therefore indicates that atmospheric effects that were insufficiently corrected in the original product were more effectively accounted for by the revised processing.

A major difference between the two processing approaches is that the original GOCI-II land SR algorithm was developed before launch using proxy observations, whereas the revised algorithm was designed using the characteristics of the actual GOCI-II sensor. The revised processing employs a GOCI-II-specific 6SV LUT for all 12 spectral bands and incorporates pixel-level observation geometry together with aerosol optical depth, water vapor, ozone, and surface elevation. These changes provide a more sensor- and observation-specific representation of atmospheric effects and are consistent with the substantial reduction in wavelength-dependent bias observed in the validation results.

The improvement was also reflected in the spectral behavior of representative surface types (Figure 5). In particular, the excessive visible reflectance observed in the original product was substantially reduced, resulting in spectral profiles that were generally more consistent with MODIS MCD19A1 for vegetation, bare soil, and urban surfaces. Nevertheless, residual discrepancies remained, particularly in the near-infrared and for some surface types. Such differences may reflect not only residual atmospheric-correction uncertainty but also differences between GOCI-II and MODIS in spectral response functions, spatial resolution, observation geometry, and the spatial representativeness of heterogeneous land surfaces. Thus, agreement with MODIS should be interpreted as inter-sensor consistency rather than absolute retrieval accuracy.

An important feature of the validation results is that the substantial reductions in bias and RMSE were not always accompanied by corresponding improvements in correlation. This discrepancy was particularly evident in the blue bands at 412 and 443 nm. As shown in Figures 5 and 6, the original GOCI-II surface reflectance exhibited pronounced positive biases relative to MODIS, particularly at shorter wavelengths and low surface reflectance levels. The revised atmospheric correction substantially reduced these systematic overestimations, resulting in markedly lower bias and RMSE. However, the remaining scatter in the improved products indicates that pixel-level variability was not reduced to the same extent. Because Pearson's correlation coefficient measures linear covariation and is insensitive to additive offsets and positive linear scaling, the reduction in systematic radiometric bias does not necessarily lead to an increase in correlation. Furthermore, differences in spectral response functions, spatial resolution, observation geometry, and residual atmospheric correction uncertainties may contribute to the remaining pixel-level discrepancies. The common-pixel analysis also confirmed that substantial reductions in bias and RMSE persisted when identical observations were compared, although changes in correlation remained band-dependent. These findings suggest that the primary improvement in the blue bands was the reduction in systematic radiometric errors rather than a uniform enhancement of pixel-to-pixel correspondence. Taken together, these results demonstrate the importance of post-launch atmospheric correction tailored to the actual spectral and observational characteristics of GOCI-II. Recent evaluations of angular correction methods for NDVI over croplands have also highlighted the influence of sun–view geometry on vegetation-index variability, suggesting that further assessment of BRDF-related uncertainties may help improve the temporal consistency of GOCI-II vegetation products [38]. The use of a fixed continental aerosol model represents a limitation of the proposed atmospheric correction algorithm. Although pixel-level GOCI-II AOD values are incorporated to account for spatial and temporal variations in aerosol loading, variations in aerosol type are not explicitly considered. Consequently, additional uncertainties may arise under atmospheric conditions dominated by dust, maritime aerosols, or mixtures of different aerosol types,

particularly in the short-wavelength bands. The GK2A/AMI surface albedo algorithm provides an example of an alternative approach that incorporates aerosol-type information derived from ECMWF CAMS data. Future studies should evaluate the sensitivity of GOCI-II surface reflectance to different aerosol models and investigate the potential benefits of incorporating spatially and temporally varying aerosol-type information into the atmospheric correction framework.

4.2. Accuracy Improvement and Valid-Pixel Availability

The substantial difference in the number of valid pixels between the original and improved products is an important consideration when interpreting their validation statistics. In the full validation dataset, the original product provided approximately 89 million valid pixel pairs per band, compared with approximately 24 million for the improved product. This reduction reflects differences in the processing and quality-screening strategies and raises the possibility that part of the apparent accuracy improvement could result from comparing different subsets of observations rather than from the revised atmospheric correction itself.

The common-pixel analysis provides a direct means of evaluating this potential sampling effect. When the comparison was restricted to approximately 24 million pixels that were simultaneously valid in the original, improved, and MODIS products, the substantial reductions in bias and RMSE were retained across all six bands. For example, RMSE was reduced by approximately 83% at both 412 and 443 nm and by approximately 71% at 490 nm. Even at longer wavelengths, where the original errors were smaller, RMSE decreased by approximately 59% at 555 nm, 25% at 660 nm, and 49% at 865 nm. These findings indicate that the reduction in validation error cannot be attributed solely to the smaller number of valid pixels retained in the improved product; a substantial component of the improvement is associated with the revised retrieval itself.

At the same time, the reduced number of valid observations represents a trade-off between retrieval accuracy and data availability. The original processing retained a much larger number of pixels, whereas the revised processing produced a smaller but more stringently screened set of observations. For an operational geostationary land product, this distinction is important because excessive screening can reduce spatial coverage even when the accuracy of individual retrievals is improved. In the operational GOCI-II land-processing framework, however, the hourly SRL and daily FVBAR products serve different purposes. The hourly SRL product prioritizes radiometric accuracy through stringent cloud screening and quality control, whereas the daily FVBAR product uses observations collected over a 16-day period for BRDF correction and temporal compositing to mitigate cloud-related data gaps. To quantitatively evaluate data availability, we compared the total numbers of valid pixels in the original and improved products throughout 2023. For each product, the valid-pixel retention rate was calculated as the ratio of the annual sum of valid pixels in the improved product to that in the original product, using hourly SRL observations and daily FVBAR products throughout 2023. The improved SRL retained approximately 31% of the valid pixels in the original version, whereas the improved daily FVBAR retained approximately 67% of those in the original FVBAR product. These results suggest that the temporal compositing framework partially mitigates the reduction in valid observations at the SRL stage, although some loss of data availability remains in the daily product.

The common-pixel results therefore support two complementary conclusions. First, the improved accuracy is not simply an artifact of differences in validation sample size, because substantial reductions in bias and RMSE remain when sampling is controlled. Second, the large reduction in the total number of valid pixels indicates that retrieval accuracy should not be considered independently of data availability. Future operational refinement should

therefore aim to preserve the demonstrated radiometric improvements while optimizing cloud and quality-screening criteria to maintain sufficient spatial and temporal coverage.

4.3. Propagation of Surface Reflectance Improvements to Downstream Land Products

The benefits of the revised surface reflectance processing were also reflected in downstream GOCI-II albedo and vegetation-index products. For surface albedo, the BRDF modeling and narrowband albedo retrieval framework was retained from the original GOCI-II algorithm, while the improved surface reflectance served as the fundamental input to the BRDF-based processing. Consequently, improvements in atmospheric correction affect the temporal BRDF characterization and the resulting narrowband black-sky and white-sky albedos. The spatial distributions of the improved narrowband albedo showed more consistent surface patterns, and the broadband albedo exhibited better agreement with MODIS MCD43A3 (Figures 7–9). Annual validation showed that the RMSE of BSA decreased from 0.037 to 0.025 and its absolute bias from 0.011 to 0.001. For WSA, the RMSE decreased from 0.039 to 0.035 and the absolute bias from 0.013 to 0.002 (Table 9).

The improvement in broadband albedo, however, should not be attributed exclusively to the revised surface reflectance. In this study, GOCI-II-specific narrow-to-broadband conversion coefficients were newly derived using 2023 GOCI-II narrowband albedo and MODIS MCD43A3 observations. Therefore, the improved broadband albedo represents the combined effects of improved upstream surface reflectance and the updated spectral conversion from narrowband to broadband albedo. This distinction is important because the BRDF and narrowband albedo formulations themselves were retained, whereas the atmospheric correction and narrow-to-broadband conversion were updated. The results therefore demonstrate how improvement of an upstream fundamental product can propagate through an operational processing chain while also showing the importance of sensor-specific parameterization at subsequent processing stages.

Despite the overall improvement, a notable exception occurred for WSA in November, when the RMSE increased markedly (Figure 9). Examination of the spatial distributions during this period showed that the largest discrepancies between GOCI-II and MODIS were concentrated primarily over northern East Asia, where MODIS exhibited extensive high-albedo surfaces. Visual inspection of the corresponding GOCI-II L1B natural-color imagery indicated that these regions were largely associated with snow-covered surfaces. The current GOCI-II albedo algorithm does not explicitly identify or separately process snow-covered surfaces, suggesting that seasonal snow cover was a likely contributor to the increased WSA uncertainty. Because snow-covered surfaces have spectral and directional reflectance characteristics that differ substantially from those of snow-free land surfaces, explicit snow detection and appropriate treatment of snow-covered pixels should be considered in future improvements. However, because snow-covered and snow-free pixels were not quantitatively separated in the present validation, the contribution of snow cover to the November anomaly cannot be determined conclusively.

A similar propagation of surface reflectance improvement was observed for the vegetation indices, for which the original NDVI and EVI formulations were retained. Compared with MODIS MOD13Q1, the NDVI RMSE decreased from 0.403 to 0.142 and the EVI RMSE from 0.274 to 0.111, while the corresponding correlations increased from 0.774 to 0.841 and from 0.577 to 0.789, respectively. Comparison with the daily GK2A/AMI vegetation indices showed an even clearer improvement: the NDVI RMSE decreased from 0.342 to 0.100 and the EVI RMSE from 0.268 to 0.071, with correlations increasing to 0.891 and 0.902, respectively (Table 10). Because the vegetation-index formulations were not modified, these improvements provide evidence that enhanced upstream surface reflectance can directly improve downstream vegetation products. The particularly strong improvement in EVI

is also physically consistent with the substantial improvement observed in the blue-band surface reflectance, which is explicitly incorporated into the EVI formulation for atmospheric resistance. Taken together, the albedo and vegetation-index results demonstrate that improving the fundamental surface reflectance product can enhance multiple downstream land products within the GOCI-II processing framework.

4.4. Limitations and Operational Implications

Several limitations should be considered when interpreting the validation results. First, the evaluation was based primarily on inter-satellite comparisons rather than direct ground-based measurements. Although MODIS MCD19A1, MCD43A3, MOD13Q1, and GK2A/AMI provide well-established reference products, differences in spectral response functions, spatial resolution, observation geometry, retrieval algorithms, and temporal sampling inevitably contribute to the observed discrepancies. The MOD13Q1 vegetation indices additionally represent a 16-day composite, whereas the GOCI-II and GK2A/AMI products have substantially higher temporal resolution. For quantitative comparisons, the last day of each MOD13Q1 compositing period was used as the temporal matching reference; however, this date does not necessarily correspond to the actual observation date contributing to the composite. Such temporal discrepancies may introduce additional uncertainties, particularly during periods of rapid vegetation change. To complement the MODIS-based evaluation, GK2A/AMI observations acquired at times corresponding to GOCI-II were also used for validation. Furthermore, the original vegetation-index time series were examined separately (Figure 11) to assess seasonal patterns without imposing identical temporal sampling. These complementary analyses help distinguish overall seasonal consistency from direct pixel-wise agreement, although uncertainties associated with spatial representativeness and inter-sensor differences remain. The validation statistics therefore represent agreement among satellite products rather than absolute retrieval accuracy.

Second, the transition from temporal minimum-reflectance compositing to observation-specific SR retrieval, together with the exclusion of pixels with missing or invalid AOD values, resulted in substantially fewer valid comparison pixels than in the original product. To control for differences in valid-pixel availability and ensure a consistent accuracy comparison between the original and revised products, an additional common-pixel validation was conducted (Table 8). The analysis demonstrated that substantial improvements in SR accuracy persisted under identical spatial sampling conditions. Nevertheless, the individual contributions of atmospheric correction and temporal compositing could not be independently quantified. Therefore, the observed accuracy improvements should be interpreted as the combined effects of the revised SR retrieval framework rather than being attributed exclusively to atmospheric correction.

In addition, the broadband albedo improvement reflects both the revised upstream surface reflectance and the newly derived GOCI-II-specific narrow-to-broadband conversion coefficients, making it difficult to isolate the individual contribution of each modification. The validation was also limited to observations acquired during 2023, and the November WSA anomaly indicates that specific seasonal surface conditions, particularly snow cover, require further investigation. An updated GOCI-II AOD retrieval algorithm is planned for operational implementation in January 2027, which is expected to reduce AOD data gaps and potentially improve the spatial coverage of subsequent SR products. However, these anticipated benefits have not yet been evaluated in the present study.

Despite these limitations, the results have direct implications for the operational use of GOCI-II land products. Unlike polar-orbiting sensors, GOCI-II provides repeated observations of East Asia from a geostationary platform, enabling land-surface conditions to be characterized at sub-daily to daily temporal scales. Improving the fundamental sur-

face reflectance product therefore benefits not only the surface reflectance itself but also multiple downstream products generated within the operational processing chain. The consistent improvements observed in surface reflectance, broadband albedo, NDVI, and EVI demonstrate the value of post-launch refinement using the actual radiometric, spectral, and observational characteristics of GOCI-II.

The improved land products and their updated Algorithm Theoretical Basis Documents (ATBDs) are scheduled to be made available through the National Ocean Satellite Center website beginning in January 2027. Their transition from algorithm development and validation to public operational service represents an important step toward the broader use of GOCI-II geostationary observations for terrestrial monitoring over East Asia. Continued evaluation after operational release, particularly across multiple years and under challenging surface and atmospheric conditions, will be important for further improving product consistency and long-term reliability.

5. Conclusions

This study demonstrated that post-launch refinement of the existing GOCI-II atmospheric correction and surface reflectance (SR) retrieval framework can substantially improve the accuracy and consistency of terrestrial products. The revised processing framework, incorporating a GOCI-II-specific 6SV LUT, pixel-level atmospheric and geometric information, and observation-specific clear-sky SR retrieval, addressed limitations associated with the original pre-launch algorithm and its temporal minimum-reflectance selection strategy.

Validation using all 12 GOCI-II Local Area slots throughout 2023 demonstrated substantial improvements in SR, particularly at shorter wavelengths. RMSE decreased from 0.271 to 0.042 at 412 nm, from 0.196 to 0.032 at 443 nm, and from 0.134 to 0.036 at 490 nm, with improvements also observed at longer wavelengths. Importantly, common-pixel validation showed that the reductions in bias and RMSE persisted when the original and improved products were evaluated using an identical set of valid pixels, confirming that the observed improvements could not be explained solely by differences in valid-pixel availability. These findings indicate that the revised processing framework effectively reduced systematic discrepancies in SR, particularly in the visible spectral region.

The benefits of the revised processing were also reflected in downstream land products. Broadband albedo showed reduced bias and RMSE, although its improvement reflects the combined effects of improved upstream SR and newly derived GOCI-II-specific narrow-to-broadband conversion coefficients. NDVI and EVI, for which the original formulations were retained, showed substantial improvements against both MODIS and GK2A/AMI reference products. These findings highlight the importance of SR quality for downstream land-product performance and demonstrate that improvements in upstream processing can contribute to greater consistency across multiple GOCI-II terrestrial products.

Despite these improvements, the evaluation identified remaining uncertainties, particularly in white-sky albedo (WSA) under seasonal snow conditions. This limitation indicates the need for improved snow detection and more appropriate treatment of snow-covered surfaces. In addition, further multi-year validation across diverse surface types, atmospheric conditions, and seasonal environments is required to assess the long-term robustness of the revised products. The improved GOCI-II land products and updated ATBDs are scheduled for operational public service through the National Ocean Satellite Center beginning in January 2027. The results provide quantitative evidence supporting the operational refinement of GOCI-II land products and their potential use in high-frequency terrestrial monitoring over East Asia.

https://doi.org/10.3390/rs18213838

Author Contributions: Conceptualization, S.-H.K.; methodology, S.-H.K. and J.C.; software, I.B. and D.S.; validation, S.-H.K., I.B., D.S. and J.C.; formal analysis, S.-H.K. and I.B.; investigation, I.B., D.S. and J.E.; data curation, I.B., D.S., J.C. and J.E.; visualization, I.B. and D.S.; writing—original draft preparation, S.-H.K., I.B., D.S.; writing—review and editing, S.-H.K., I.B., D.S., J.C. and J.E.; supervision, S.-H.K. and J.E.; project administration, S.-H.K. and J.E.; funding acquisition, S.-H.K. All authors have read and agreed to the published version of the manuscript.

Funding: This research was supported by Korea Institute of Marine Science & Technology Promotion (KIMST) funded by the Ministry of Oceans and Fisheries (RS-2022-KS221660).

Data Availability Statement: The satellite datasets used in this study are available from their respective data providers, including the National Ocean Satellite Center (NOSC), the National Meteorological Satellite Center (NMSC), and NASA MODIS data services. The improved GOCI-II land products and updated Algorithm Theoretical Basis Documents (ATBDs) are scheduled to become publicly available through the NOSC beginning in January 2027.

Acknowledgments: During the preparation of this manuscript, the authors used ChatGPT (GPT-5.6, OpenAI, San Francisco, CA, USA) for English-language editing and improvement of clarity and readability. The authors reviewed and edited the output and take full responsibility for the content of this publication.

Conflicts of Interest: All authors are employees of PERPIXEL Inc. The authors declare that they have no other commercial or financial relationships that could be construed as potential conflicts of interest.

References

1. Vermote, E.F.; El Saleous, N.Z.; Justice, C.O. Atmospheric correction of MODIS data in the visible to middle infrared: First results. *Remote Sens. Environ.* **2002**, *83*, 97–111. [CrossRef]
2. Vermote, E.; Justice, C.; Claverie, M.; Franch, B. Preliminary analysis of the performance of the Landsat 8/OLI land surface reflectance product. *Remote Sens. Environ.* **2016**, *185*, 46–56. [CrossRef]
3. Schaaf, C.B.; Gao, F.; Strahler, A.H.; Lucht, W.; Li, X.; Tsang, T.; Strugnell, N.C.; Zhang, X.; Jin, Y.; Muller, J.-P.; et al. First operational BRDF, albedo nadir reflectance products from MODIS. *Remote Sens. Environ.* **2002**, *83*, 135–148. [CrossRef]
4. Lucht, W.; Schaaf, C.B.; Strahler, A.H. An algorithm for the retrieval of albedo from space using semiempirical BRDF models. *IEEE Trans. Geosci. Remote Sens.* **2000**, *38*, 977–998. [CrossRef]
5. Liang, S. Narrowband to broadband conversions of land surface albedo I: Algorithms. *Remote Sens. Environ.* **2001**, *76*, 213–238. [CrossRef]
6. Tucker, C.J. Red and photographic infrared linear combinations for monitoring vegetation. *Remote Sens. Environ.* **1979**, *8*, 127–150. [CrossRef]
7. Huete, A.; Didan, K.; Miura, T.; Rodriguez, E.P.; Gao, X.; Ferreira, L.G. Overview of the radiometric and biophysical performance of the MODIS vegetation indices. *Remote Sens. Environ.* **2002**, *83*, 195–213. [CrossRef]
8. Justice, C.O.; Román, M.O.; Csiszar, I.; Vermote, E.F.; Wolfe, R.E.; Hook, S.J.; Friedl, M.; Wang, Z.; Schaaf, C.B.; Miura, T.; et al. Land and cryosphere products from Suomi NPP VIIRS: Overview and status. *J. Geophys. Res. Atmos.* **2013**, *118*, 9753–9765. [CrossRef]
9. Moravec, D.; Komárek, J.; López-Cuervo Medina, S.; Molina, I. Effect of Atmospheric Corrections on NDVI: Intercomparability of Landsat 8, Sentinel-2, and UAV Sensors. *Remote Sens.* **2021**, *13*, 3550. [CrossRef]
10. Doxani, G.; Vermote, E.; Roger, J.-C.; Gascon, F.; Adriaensen, S.; Frantz, D.; Hagolle, O.; Hollstein, A.; Kirches, G.; Li, F.; et al. Atmospheric Correction Inter-comparison eXercise. *Remote Sens.* **2018**, *10*, 352. [CrossRef]
11. Vermote, E.F.; Tanré, D.; Deuzé, J.L.; Herman, M.; Morcrette, J.J. Second Simulation of the Satellite Signal in the Solar Spectrum, 6S: An overview. *IEEE Trans. Geosci. Remote Sens.* **1997**, *35*, 675–686. [CrossRef]
12. Kotchenova, S.Y.; Vermote, E.F.; Matarrese, R.; Klemm, F.J. Validation of a vector version of the 6S radiative transfer code for atmospheric correction of satellite data. Part I: Path radiance. *Appl. Opt.* **2006**, *45*, 6762–6774. [CrossRef]
13. Fraser, R.S.; Kaufman, Y.J. The relative importance of aerosol scattering and absorption in remote sensing. *IEEE Trans. Geosci. Remote Sens.* **1985**, *GE-23*, 625–633. [CrossRef]
14. Lyapustin, A.; Martonchik, J.; Wang, Y.; Laszlo, I.; Korkin, S. Multiangle implementation of atmospheric correction (MAIAC): 1. Radiative transfer basis and look-up tables. *J. Geophys. Res. Atmos.* **2011**, *116*, D03210. [CrossRef]
15. Lyapustin, A.; Wang, Y.; Korkin, S.; Huang, D. MODIS Collection 6 MAIAC algorithm. *Atmos. Meas. Tech.* **2018**, *11*, 5741–5765. [CrossRef]

16. Doxani, G.; Vermote, E.F.; Roger, J.-C.; Skakun, S.; Gascon, F.; Collison, A.; De Keukelaere, L.; Desjardins, C.; Frantz, D.; Hagolle, O.; et al. Atmospheric Correction Inter-comparison eXercise, ACIX-II Land: An Assessment of Atmospheric Correction Processors for Landsat 8 and Sentinel-2 over Land. *Remote Sens. Environ.* **2023**, *285*, 113412. [CrossRef]
17. Colin, J.; Hagolle, O.; Landier, L.; Coustance, S.; Kettig, P.; Meygret, A.; Osman, J.; Vermote, E. Assessment of the Performance of the Atmospheric Correction Algorithm MAJA for Sentinel-2 Surface Reflectance Estimates. *Remote Sens.* **2023**, *15*, 2665. [CrossRef]
18. Carrer, D.; Ceamanos, X.; Six, B.; Roujean, J.-L. AERUS-GEO: A newly available satellite-derived aerosol optical depth product over Europe and Africa. *Geophys. Res. Lett.* **2014**, *41*, 7731–7738. [CrossRef]
19. Li, S.; Wang, W.; Hashimoto, H.; Xiong, J.; Vandal, T.; Yao, J.; Qian, L.; Ichii, K.; Lyapustin, A.; Wang, Y.; et al. First provisional land surface reflectance product from geostationary satellite Himawari-8 AHI. *Remote Sens.* **2019**, *11*, 2990. [CrossRef]
20. Wang, W.; Wang, Y.; Lyapustin, A.; Hashimoto, H.; Park, T.; Michaelis, A.; Nemani, R. A Novel Atmospheric Correction Algorithm to Exploit the Diurnal Variability in Hypertemporal Geostationary Observations. *Remote Sens.* **2022**, *14*, 964. [CrossRef]
21. Li, W.; Ichii, K.; Zhang, B.; Yamamoto, Y.; Yang, W.; Miura, T.; Yoshioka, H.; Matsuoka, M.; Obata, K.; Sharma, R.C.; et al. Estimation and Evaluation of Land Surface Reflectance from a Next-Generation Geostationary Meteorological Satellite, Himawari-8/9 AHI. *J. Meteorol. Soc. Jpn.* **2025**, *103*, 87–109. [CrossRef]
22. Zhang, B.; Ichii, K.; Li, W.; Yamamoto, Y.; Yang, W.; Sharma, R.C.; Yoshioka, H.; Obata, K.; Matsuoka, M.; Miura, T. Evaluation of Himawari-8/AHI land surface reflectance at mid-latitudes using LEO sensors with off-nadir observation. *Remote Sens. Environ.* **2025**, *316*, 114491. [CrossRef]
23. Miura, T.; Nagai, S.; Takeuchi, M.; Ichii, K.; Yoshioka, H. Improved characterisation of vegetation and land surface seasonal dynamics in Central Japan with Himawari-8 hypertemporal data. *Sci. Rep.* **2019**, *9*, 15692. [CrossRef]
24. He, T.; Zhang, Y.; Liang, S.; Yu, Y.; Wang, D. Developing Land Surface Directional Reflectance and Albedo Products from Geostationary GOES-R and Himawari Data: Theoretical Basis, Operational Implementation, and Validation. *Remote Sens.* **2019**, *11*, 2655. [CrossRef]
25. Roujean, J.-L.; Leroy, M.; Deschamps, P.-Y. A bidirectional reflectance model of the Earth's surface for the correction of remote sensing data. *J. Geophys. Res. Atmos.* **1992**, *97*, 20455–20468. [CrossRef]
26. Lee, C.S.; Han, K.-S.; Yeom, J.-M.; Lee, K.-S.; Seo, M.; Hong, J.; Hong, J.-W.; Lee, K.; Shin, J.; Shin, I.-C.; et al. Surface albedo from the geostationary Communication, Ocean and Meteorological Satellite (COMS)/Meteorological Imager (MI) observation system. *GISci. Remote Sens.* **2018**, *55*, 38–62. [CrossRef]
27. Sim, S.; Choi, S.; Jung, D.; Woo, J.; Kim, N.; Park, S.; Kim, H.; Jeong, U.; Hong, H.; Han, K.-S. Retrieval of pseudo-BRDF-adjusted surface reflectance at 440 nm from the Geostationary Environmental Monitoring Spectrometer (GEMS). *Atmos. Meas. Tech.* **2024**, *17*, 5601–5618. [CrossRef]
28. Lu, J.; He, T.; Song, D.-X.; Wang, C.-Q. Using Geostationary Satellite Observations to Improve the Monitoring of Vegetation Phenology. *Remote Sens.* **2024**, *16*, 2173. [CrossRef]
29. Yeom, J.-M.; Kim, H.-O. Comparison of NDVIs from GOCI and MODIS data towards improved assessment of crop temporal dynamics in the case of paddy rice. *Remote Sens.* **2015**, *7*, 11326–11343. [CrossRef]
30. Yeom, J.-M.; Roujean, J.-L.; Han, K.-S.; Lee, K.-S.; Kim, H.-W. Thin cloud detection over land using background surface reflectance based on the BRDF model applied to Geostationary Ocean Color Imager (GOCI) satellite data sets. *Remote Sens. Environ.* **2020**, *239*, 111610. [CrossRef]
31. Lee, K.-S.; Lee, E.; Jin, D.; Seong, N.-H.; Jung, D.; Sim, S.; Han, K.-S. Retrieval and uncertainty analysis of land surface reflectance using a Geostationary Ocean Color Imager. *Remote Sens.* **2022**, *14*, 360. [CrossRef]
32. Choi, M.; Kim, J.; Lee, J.; Kim, M.; Park, Y.-J.; Holben, B.; Eck, T.F.; Li, Z.; Song, C.H. GOCI Yonsei aerosol retrieval version 2 products: An improved algorithm and error analysis with uncertainty estimation from 5-year validation over East Asia. *Atmos. Meas. Tech.* **2018**, *11*, 385–408. [CrossRef]
33. Han, K.-S.; Lee, K.-S.; Choi, S.; Seong, N. BRDF/Albedo/NDVI/EVI Algorithm for GOCI-II Data: Algorithm Theoretical Basis Document (ATBD). GOCI-II Ground Segment System, Version 1.1, 7 May 2021. National Ocean Satellite Center, Korea Hydrographic and Oceanographic Agency. Available online: https://nosc.go.kr/board/actionBoardListBoard0009.do (accessed on 1 September 2026).
34. Chen, Y.; Mu, X.; McVicar, T.R.; Wang, Y.; Guo, Y.; Yan, K.; Lai, Y.; Xie, D.; Yan, G. Using an improved radiative transfer model to estimate leaf area index, fractional vegetation cover and leaf inclination angle from Himawari-8 geostationary satellite data. *Remote Sens. Environ.* **2025**, *318*, 114595. [CrossRef]
35. Lee, K.-H.; Lee, K.-S. Surface Reflectance Algorithm for GOCI-II Data: Algorithm Theoretical Basis Document (ATBD). GOCI-II Ground Segment System, Version 0.5, 7 May 2021. National Ocean Satellite Center, Korea Hydrographic and Oceanographic Agency. Available online: https://nosc.go.kr/board/actionBoardListBoard0009.do (accessed on 1 September 2026).
36. Lee, C.S.; Yeom, J.M.; Lee, H.L.; Kim, J.J.; Han, K.S. Sensitivity Analysis of 6S-Based Look-Up Table for Surface Reflectance Retrieval. *Asia-Pac. J. Atmos. Sci.* **2015**, *51*, 91–101. [CrossRef]

37. Lee, H.-S.; Lee, K.-S. Operational Atmospheric Correction Method over Land Surfaces for GOCI Images. *Korean J. Remote Sens.* **2018**, *34*, 127–139. [CrossRef]
38. Guo, Y.; Mu, X.; Lyu, X.; Fan, D.; Lei, C.; Xie, D.; Yan, G. Evaluating the correction methods for NDVI angular effect based on decametric resolution BRDF observations over cropland. *Remote Sens. Environ.* **2026**, *339*, 115403. [CrossRef]

Disclaimer/Publisher's Note: The statements, opinions and data contained in all publications are solely those of the individual author(s) and contributor(s) and not of MDPI and/or the editor(s). MDPI and/or the editor(s) disclaim responsibility for any injury to people or property resulting from any ideas, methods, instructions or products referred to in the content.